

Hydrodynamic interactions of spherical particles in Poiseuille flow between two parallel walls

S. Bhattacharya,¹ J. Bławdziewicz,¹ and E. Wajnryb^{1,2}

¹*Department of Mechanical Engineering, Yale University, P.O. Box 20-8286, New Haven, CT 06520*

²*On leave from IPPT Warsaw, Poland*

(Dated: August 21, 2018)

We study hydrodynamic interactions of spherical particles in incident Poiseuille flow in a channel with infinite planar walls. The particles are suspended in a Newtonian fluid, and creeping-flow conditions are assumed. Numerical results, obtained using our highly accurate Cartesian-representation algorithm [Physica A xxx, xx, 2005], are presented for a single sphere, two spheres, and arrays of many spheres. We consider the motion of freely suspended particles as well as the forces and torques acting on particles adsorbed at a wall. We find that the pair hydrodynamic interactions in this wall-bounded system have a complex dependence on the lateral interparticle distance due to the combined effects of the dissipation in the gap between the particle surfaces and the back-flow associated with the presence of the walls. For immobile particle pairs we have examined the crossover between several far-field asymptotic regimes corresponding to different relations between the particle separation and the distances of the particles from the walls. We have also shown that the cumulative effect of the far-field flow substantially influences the force distribution in arrays of immobile spheres. Therefore, the far-field contributions must be included in any reliable algorithm for evaluating many-particle hydrodynamic interactions in the parallel-wall geometry.

I. INTRODUCTION

In his pioneering work (more than eighty years ago) Faxén [1] considered motion of a spherical particle suspended in a fluid confined by two parallel walls. A recent, considerable interest in particle motion in confined geometries has been stimulated by development of new experimental techniques [2, 3, 4, 5, 6, 7] and by emerging applications, such as the microfluidic devices [8] and technologies for production of microstructured materials by a self-assembly process [9, 10].

There have been published a number of fundamental experimental and numerical studies on particle dynamics in channels with parallel planar walls for suspensions of Brownian [11, 12, 13, 14, 15, 16, 17, 18, 19, 20] and non-Brownian [21, 22, 23, 24, 25] particles. Some of these studies focused on quasi-two-dimensional phenomena [12, 13, 14, 16, 17, 19], and some on bulk properties, such as particle migration in the pressure-driven [21, 22, 23, 25] or shear [24] flow.

Quantitative numerical studies of wall-bounded suspensions require efficient methods for evaluation of multiparticle hydrodynamic interactions in these systems. Some interesting numerical results were obtained with the help of the wall-superposition approximation [13, 14] or by modeling the walls as arrays of immobile spheres [21, 22, 23, 24, 25]. These approaches seem sufficient for describing certain qualitative features of wall-bounded suspensions (e.g., in Stokesian-dynamic simulations of hydrodynamic particle diffusion) but the accuracy of such approximations is often unknown. Moreover, in some cases, they entirely miss certain important phenomena. For example, the superposition approximation reproduces neither the large transverse resistance coefficient of rigid arrays of spheres [26] nor the enhanced relative transverse particle motion, observed by Cui *et*

al. [19] and independently predicted by our recent analysis [27].

To overcome these difficulties, we have developed an accurate Cartesian-representation method for evaluation of multiparticle hydrodynamic interactions in wall-bounded suspensions of spheres [26]. (A related approach was also independently proposed by Jones [28].) Our method relies on expanding the flow in a wall-bounded system using two basis sets of Stokes flows. The spherical basis set of multipolar flows is used to describe the interaction of the fluid with the particles, and the Cartesian basis set is used to account for the presence of the walls.

In our previous studies, the Cartesian-representation method was applied to determine the resistance functions for systems of spheres in quiescent fluid [26, 27, 29]. In the present paper we extend these results to suspensions in a pressure-driven external flow. We note that the one-particle motion in such a system was investigated by Jones [28] and Staben *et al.* [30] but, to our knowledge, no accurate multiparticle results have been reported so far.

This paper is organized as follows. In Sec. II the system is defined, and in Sec. III the Cartesian-representation method is summarized. Our numerical results for single-particle, two-particle, and multiparticle systems are described in Sec. IV. Conclusions are presented in Sec. V.

II. PARTICLES IN PARABOLIC FLOW

We consider a suspension of N spherical particles of diameter $d = 2a$ in creeping flow between two parallel planar walls. The no-slip boundary conditions are satisfied on the walls and the particle surfaces. The walls are in the planes $z = 0$ and $z = H$, where H denotes the wall separation, and (x, y, z) are the Cartesian coor-

dinates. The position of the center of particle i (where $i = 1, \dots, N$) is denoted by \mathbf{R}_i , and its translational and rotational velocities are \mathbf{U}_i and $\mathbf{\Omega}_i$, respectively. The external forces and torques acting on particle i are denoted by \mathcal{F}_i and \mathcal{T}_i .

In this paper we focus on particle motion in an imposed parabolic flow of the form

$$\mathbf{v}^{\text{ext}} = 4U_p \frac{z}{H} \left(1 - \frac{z}{H}\right) \hat{\mathbf{e}}_x, \quad (1)$$

where U_p is the flow amplitude, and $\hat{\mathbf{e}}_x$ is the unit vector along the x coordinate. The forces and torques on immobile particles with

$$\mathbf{U}_i = 0, \quad \mathbf{\Omega}_i = 0, \quad (2)$$

can be represented by the resistance formula

$$\begin{bmatrix} \mathcal{F}_i \\ \mathcal{T}_i \end{bmatrix} = - \begin{bmatrix} \zeta_i^{\text{tp}} \\ \zeta_i^{\text{rp}} \end{bmatrix} U_p. \quad (3)$$

Similarly, the velocities of freely suspended particles with

$$\mathcal{F}_i = 0, \quad \mathcal{T}_i = 0, \quad (4)$$

can be represented by the mobility formula

$$\begin{bmatrix} \mathbf{U}_i \\ \mathbf{\Omega}_i \end{bmatrix} = \begin{bmatrix} \nu_i^{\text{tp}} \\ \nu_i^{\text{rp}} \end{bmatrix} U_p. \quad (5)$$

In our considerations we assume that the applied flow (1) is in the x direction. Thus, the resistance coefficients ζ_i^{tp} and ζ_i^{rp} and the mobility coefficients ν_i^{tp} and ν_i^{rp} are vectors. For the external parabolic flow applied in an arbitrary lateral direction, the corresponding resistance and mobility coefficients have a tensorial character.

Condition (4) can be obtained by applying to immobile particles the forces and torques opposite to those given by equation (3). Thus, the resistance and mobility coefficients ζ and ν satisfy the following relation

$$\begin{bmatrix} \nu_i^{\text{tp}} \\ \nu_i^{\text{rp}} \end{bmatrix} = \sum_{j=1}^N \begin{bmatrix} \mu_{ij}^{\text{tt}} & \mu_{ij}^{\text{tr}} \\ \mu_{ij}^{\text{rt}} & \mu_{ij}^{\text{rr}} \end{bmatrix} \cdot \begin{bmatrix} \zeta_j^{\text{tp}} \\ \zeta_j^{\text{rp}} \end{bmatrix}, \quad (6)$$

where μ_{ij}^{AB} ($A, B = \text{t}, \text{r}$) are the translational and rotational components of the usual mobility matrix [31] for a system of particles in quiescent fluid between the walls. The many-particle translational–rotational mobility matrix μ_{ij}^{AB} is the inverse of the corresponding multi-particle resistance matrix ζ_{ij}^{AB} , i.e.,

$$\sum_{j=1}^N \begin{bmatrix} \mu_{ij}^{\text{tt}} & \mu_{ij}^{\text{tr}} \\ \mu_{ij}^{\text{rt}} & \mu_{ij}^{\text{rr}} \end{bmatrix} \cdot \begin{bmatrix} \zeta_{jk}^{\text{tt}} & \zeta_{jk}^{\text{tr}} \\ \zeta_{jk}^{\text{rt}} & \zeta_{jk}^{\text{rr}} \end{bmatrix} = \begin{bmatrix} \hat{\mathbf{I}} & 0 \\ 0 & \hat{\mathbf{I}} \end{bmatrix}, \quad (7)$$

where $\hat{\mathbf{I}}$ is the identity tensor.

In our recent publications [26, 27, 29] we have introduced a formalism that allows us to efficiently evaluate

the translational–rotational mobility matrix μ for a system of spherical particles confined between two parallel walls. In the present paper our method is used to evaluate the friction and mobility matrices ζ_i^{AP} and ν_i^{AP} ($A = \text{t}, \text{r}$) associated with the Poiseuille flow between the walls.

III. CARTESIAN AND HELE–SHAW REPRESENTATION METHODS

In this section we summarize the key elements of our Cartesian-representation method for evaluating the hydrodynamic friction and mobility matrices in a suspension confined between two parallel walls. We also outline our asymptotic results, which rely on expansion of the far field flow into a Hele–Shaw basis. The asymptotic results apply for sufficiently large interparticle separations.

A detailed description of our technique is presented in [26] and in [29]. The Hele–Shaw basis and its relation to the spherical basis [32] used in our analysis [26] is summarized in Appendices A and B.

A. Induced-force formulation

In our approach, the effect of the suspended particles on the surrounding fluid is represented in terms of the induced-force distributions on the particle surfaces

$$\mathbf{F}_i(\mathbf{r}) = a^{-2} \delta(r_i - a) \mathbf{f}_i(\mathbf{r}), \quad (8)$$

where

$$\mathbf{r}_i = \mathbf{r} - \mathbf{R}_i \quad (9)$$

and $r_i = |\mathbf{r}_i|$. By definition of the induced force, the flow field

$$\mathbf{v}(\mathbf{r}) = \mathbf{v}^{\text{ext}}(\mathbf{r}) + \sum_{i=1}^N \int \mathbf{T}(\mathbf{r}, \mathbf{r}') \cdot \mathbf{F}_i(\mathbf{r}') \, d\mathbf{r}' \quad (10)$$

is identical to the velocity field in the presence of the particles [33, 34, 35]. Here

$$\mathbf{T}(\mathbf{r}, \mathbf{r}') = \mathbf{T}_0(\mathbf{r} - \mathbf{r}') + \mathbf{T}'(\mathbf{r}, \mathbf{r}') \quad (11)$$

is the Green's function for the Stokes flow in the wall-bounded system, $\mathbf{T}_0(\mathbf{r})$ is the Oseen tensor (free-space Green's function), and $\mathbf{T}'(\mathbf{r}, \mathbf{r}')$ describes the flow reflected from the walls.

For a system of particles moving with the translational and angular velocities \mathbf{U}_i and $\mathbf{\Omega}_i$ in the external flow \mathbf{v}^{ext} , the induced-force distribution (8) can be obtained from the boundary-integral equation of the form

$$\begin{aligned} & [\mathbf{Z}_i^{-1} \mathbf{F}_i](\mathbf{r}) + \sum_{j=1}^N \int [(1 - \delta_{ij}) \mathbf{T}_0(\mathbf{r} - \mathbf{r}') \\ & + \mathbf{T}'(\mathbf{r}, \mathbf{r}') \cdot \mathbf{F}_j(\mathbf{r}') \, d\mathbf{r}' = \mathbf{v}_i^{\text{rb}}(\mathbf{r}) - \mathbf{v}^{\text{ext}}(\mathbf{r}), \\ & \mathbf{r} \in S_i, \end{aligned} \quad (12)$$

where the rigid-body velocity field

$$\mathbf{v}_i^{\text{rb}}(\mathbf{r}) = \mathbf{U}_i + \boldsymbol{\Omega}_i \times \mathbf{r}_i \quad (13)$$

and the external flow field $\mathbf{v}^{\text{ext}}(\mathbf{r})$ are evaluated on the surface S_i of particle i . In the boundary-integral equation (12), \mathbf{Z}_i denotes the one-particle scattering operator, which is defined by the relation

$$\mathbf{F}_i = -\mathbf{Z}_i(\mathbf{v}_i^{\text{in}} - \mathbf{v}_i^{\text{rb}}), \quad (14)$$

where \mathbf{v}_i^{in} is the velocity incident to particle i . For specific particle models, explicit expressions for the operator \mathbf{Z}_i are known [32, 36, 37].

The force and torque acting on particle i can be evaluated from the induced-force distribution using the integrals

$$\mathcal{F}_i = \int \mathbf{F}_i(\mathbf{r}) \, d\mathbf{r}, \quad \mathcal{T}_i = \int \mathbf{r}_i \times \mathbf{F}_i(\mathbf{r}) \, d\mathbf{r}. \quad (15)$$

The friction matrix (3) can be computed by solving the boundary equation (12) with the external flow \mathbf{v}^{ext} in the form (1) and no rigid-body motion, $\mathbf{v}_i^{\text{rb}} = 0$. Similarly, the translational-rotational friction matrix is obtained by solving (12) with a nonzero rigid-body motion (13) and no external flow, $\mathbf{v}^{\text{ext}} = 0$.

B. Multipolar expansion

In our approach, the boundary-integral equation (12) is solved after transforming it into a linear matrix equation. The transformation is achieved by projecting (12)

onto a spherical basis of Stokes flows. We use here the multipolar representation introduced by Cichocki *et al.* [32], but we apply a different normalization to emphasize full symmetry of the problem [26, 27].

Accordingly, the induced-force distributions at the surfaces of particles $i = 1 \dots N$ are expanded using the basis set of multipolar force distributions $\mathbf{w}_{lm\sigma}^+(\mathbf{r}_i)$. Similarly, the flows incoming to each particle are expanded into the nonsingular basis set of Stokes flows $\mathbf{v}_{lm\sigma}^+(\mathbf{r}_i)$. Here l and m are the angular and azimuthal spherical-harmonics orders, and $\sigma = 0, 1, 2$ characterizes the type of the flow. Explicit definitions of the basis sets $\mathbf{w}_{lm\sigma}^+$ and $\mathbf{v}_{lm\sigma}^+$ (as well as their counterparts $\mathbf{w}_{lm\sigma}^-$ and $\mathbf{v}_{lm\sigma}^-$ that correspond to singular Stokes flows) are given in [26, 32].

In order to obtain the multipolar representation of the boundary-integral equation (12), we apply the multipolar expansion

$$\mathbf{F}_i(\mathbf{r}) = \sum_{lm\sigma} f_i(lm\sigma) a^{-2} \delta(r_i - a) \mathbf{w}_{lm\sigma}^+(\mathbf{r}_i) \quad (16)$$

to the induced-force density (8). The external flow relative to the particle motion is similarly expanded,

$$\mathbf{v}_i^{\text{rb}}(\mathbf{r}) - \mathbf{v}^{\text{ext}}(\mathbf{r}) = \sum_{lm\sigma} c_i(lm\sigma) \mathbf{v}_{lm\sigma}^+(\mathbf{r}_i). \quad (17)$$

Inserting these expansions into Eq. (12) yields a linear equation of the form

$$\sum_{j=1}^N \sum_{l'm'\sigma'} M_{ij}(lm\sigma | l'm'\sigma') f_j(l'm'\sigma') = c_i(lm\sigma), \quad (18)$$

where the matrix M can be decomposed as

$$M_{ij}(lm\sigma | l'm'\sigma') = \delta_{ij} \delta_{ll'} \delta_{mm'} Z_i^{-1}(l; \sigma | \sigma') + (1 - \delta_{ij}) G_{ij}^0(lm\sigma | l'm'\sigma') + G'_{ij}(lm\sigma | l'm'\sigma'). \quad (19)$$

The first term on the right side of the above expression corresponds to the single-particle scattering operator \mathbf{Z}_i^{-1} in equation (12); the second one to the integral operator with the kernel \mathbf{T}_0 , and the third one to the integral operator with the kernel \mathbf{T}' . Explicit expressions for the first two terms were derived by Felderhof and his collaborators [32, 36, 38] some time ago. Quadrature relations [26, 27] and asymptotic formulas [29] for the wall contribution G'_{ij} were recently derived by our group (as discussed in Sec. III D below).

C. Friction and mobility of spheres in parabolic flow

In order to evaluate the resistance tensors ζ_i^{tp} and ζ_i^{rp} for immobile particles in Poiseuille flow, Eq. (18) is solved

with the right-hand side corresponding to the velocity field (1). The resulting induced-force multipolar distributions (16) are projected onto the total force and torque using expressions (15). The solution can be conveniently expressed in terms of the grand friction matrix

$$\mathbf{F} = \mathbf{M}^{-1}, \quad (20)$$

which is inverse to the grand mobility matrix \mathbf{M} with the elements given by Eq. (19).

As shown in [26], the translational-rotational friction matrix ζ_{ij}^{AB} ($A, B = \text{t, r}$) is given by the relation

$$\zeta_{ij}^{AB} = \sum_{lm\sigma} \sum_{l'm'\sigma'} \mathbf{X}(A | lm\sigma) F_{ij}(lm\sigma | l'm'\sigma') \mathbf{X}(l'm'\sigma' | B). \quad (21)$$

Here $F_{ij}(lm\sigma | l'm'\sigma')$ are the elements of the grand friction matrix (20), and $\mathbf{X}(A | lm\sigma) = \mathbf{X}^*(lm\sigma | A)$ are

the elements of projection matrices onto the subspace of translational ($l = 1, \sigma = 0$) and rotational ($l = 1, \sigma = 1$) rigid-body motions. Explicit expressions for these

matrices are listed in Appendix B of Ref. 26.

The resistance coefficients ζ_i^{Ap} ($A = t, r$) are given by a relation analogous to (21),

$$\zeta_i^{Ap} = \sum_{j=1}^N \sum_{lm\sigma} \sum_{l'm'\sigma'} \mathbf{X}(A | lm\sigma) F_{ij}(lm\sigma | l'm'\sigma') Y_j(l'm'\sigma' | p), \quad (22)$$

where $Y_j(l'm'\sigma' | p)$ are the elements of the matrix representing the orthogonal projection onto the subspace of pressure-driven flows (1). Relation (22) and explicit expressions for the matrix $Y_j(l'm'\sigma' | p)$ are derive in Appendix C. We note that, unlike Eq. (21), relation (22) involves summation over the particles. This summation is needed because the external parabolic flow (1) is applied to all particles in the system.

D. Cartesian representation

To determine the resistance coefficients (21) and (22), the matrix (19) in the force-multipole equation (18) has to be first evaluated. Explicit expressions for the single-particle scattering matrix Z_i^{-1} and the free-space contribution G_{ij}^0 are known [32, 38]. To evaluate the wall contribution G'_{ij} to the matrix (19) we employ our recently developed Cartesian-representation method [26]. For sufficiently large interparticle separations appropriate asymptotic expressions [29] can also be used.

As explained in [26, 27], the Cartesian-representation method relies on transformations between the spherical basis sets of Stokes flows $\mathbf{v}_{lm\sigma}^\pm$ and the Cartesian basis sets $\mathbf{v}_{\mathbf{k}\sigma}^\pm$ (where \mathbf{k} is a lateral wave vector). According to the discussion in Sec. III C, the multipolar spherical sets $\mathbf{v}_{lm\sigma}^\pm$ correspond to an expansion of the velocity field into spherical harmonics. Due to symmetry, the matrix Z_i , describing interaction of the flow field with a spherical particle, is thus diagonal in the spherical-harmonics orders l and m . The Cartesian basis sets correspond to an expansion of the velocity field into lateral Fourier modes. In the Cartesian representation the matrix Z_w that describes interaction of the flow with a wall is diagonal in the wave vector \mathbf{k} . This diagonal structure of the scattering matrices Z_i and Z_w yields a significant simplification of the problem.

To express our results in a compact form, we introduce a matrix notation in the three-dimensional linear space with the components corresponding to the indices $\sigma = 0, 1, 2$ that identify the tensorial character of the basis flow fields $\mathbf{v}_{lm\sigma}^\pm$. In this notation, a column vector with components $a(\sigma)$ is denoted by \mathbf{a} , and a matrix with elements $A(\sigma | \sigma')$ is denoted by \mathbf{A} . Accordingly, the column vectors associated with the coef-

ficients $f_i(lm\sigma)$ and $c_i(lm\sigma)$ are represented by $\mathbf{f}_i(lm)$ and $\mathbf{c}_i(lm)$, and the two-wall Green's matrix with the elements $G'_{ij}(lm\sigma | l'm'\sigma')$ is represented by $\mathbf{G}'_{ij}(lm | l'm')$. We will also use 3×6 , 6×6 and 6×3 matrices composed of 3×3 blocks, as indicated below.

Our result for the wall Green's matrix G'_{ij} can be expressed in terms of the following Fourier integral

$$\mathbf{G}'_{ij}(lm | l'm') = \int d\mathbf{k} \tilde{\Psi}(\mathbf{k}; Z_i, Z_j, H) e^{\mathbf{k} \cdot \mathbf{e}_{ij}}, \quad (23)$$

where $\mathbf{e}_{ij} = X_{ij}\hat{\mathbf{e}}_x + Y_{ij}\hat{\mathbf{e}}_y$ is the projection of the vector $\mathbf{R}_{ij} = \mathbf{R}_i - \mathbf{R}_j$ onto the x - y plane, and $\mathbf{k} = k_x\hat{\mathbf{e}}_x + k_y\hat{\mathbf{e}}_y$ is the corresponding two-dimensional wave vector. The matrix $\tilde{\Psi}$ in the above expression depends on the wall separation H and the vertical coordinates Z_i and Z_j of the points i and j (measured with respect to the position of the lower wall). This matrix is a product of several simple matrices,

$$\begin{aligned} \tilde{\Psi}(\mathbf{k}; Z_i, Z_j, H) = & -\eta^{-1} \mathbf{T}_{\text{SC}}(lm, \mathbf{k}) \cdot \tilde{\mathbf{S}}_{\text{iW}}(\mathbf{k}) \cdot \tilde{\mathbf{Z}}_{\text{TW}}(\mathbf{k}) \\ & \cdot \tilde{\mathbf{S}}_{\text{wJ}}(\mathbf{k}) \cdot \mathbf{T}_{\text{CS}}(\mathbf{k}, l'm'), \end{aligned} \quad (24)$$

where η is the fluid viscosity.

The component matrices

$$\mathbf{T}_{\text{CS}}(\mathbf{k}, lm) = [\mathbf{T}_{\text{SC}}(lm, \mathbf{k})]^\dagger = \begin{bmatrix} \mathbf{T}_{\text{CS}}^{+-}(\mathbf{k}, lm) \\ \mathbf{T}_{\text{CS}}^{-+}(\mathbf{k}, lm) \end{bmatrix} \quad (25)$$

describe the transformations between the spherical (S) and Cartesian (C) basis fields. The superscripts \pm refer to the singular and nonsingular basis fields for the spherical basis, and the fields that exponentially grow (+) or decay (-) in the vertical direction z for the Cartesian basis. The matrices (25) consist of two 3×3 blocks corresponding to the lower and the upper wall, respectively.

Next, the matrices

$$\tilde{\mathbf{S}}_{\text{wS}}(\mathbf{k}) = [\tilde{\mathbf{S}}_{\text{sW}}(\mathbf{k})]^\dagger = \begin{bmatrix} \tilde{\mathbf{S}}_{\text{C}}^{++}(kZ_{\text{L}s}) & 0 \\ 0 & \tilde{\mathbf{S}}_{\text{C}}^{--}(kZ_{\text{U}s}) \end{bmatrix} \quad (26)$$

correspond to the propagation of the Cartesian flow-field components between the point $s = i, j$ and the lower (L) and upper (U) walls. Here $Z_{\text{L}s} = -Z_s$ and $Z_{\text{U}s} = H - Z_s$

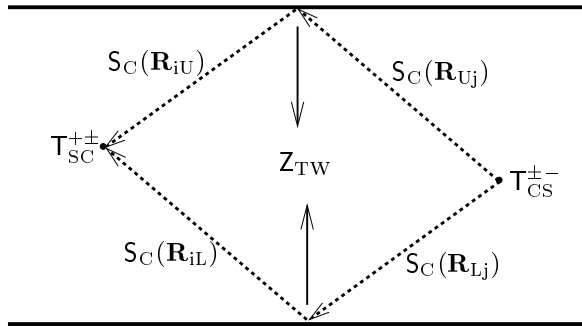


FIG. 1: Schematic representation of Eq. (24). The vectors \mathbf{R}_{Aj} and \mathbf{R}_{iA} represent the relative position of the particle $k = i, j$ and the lower ($A = L$) or upper ($A = U$) wall.

are the relative vertical coordinates of the point s with respect to the walls.

Finally, the matrix

$$\tilde{\mathbf{Z}}_{\text{TW}}(\mathbf{k}) = \begin{bmatrix} \mathbf{Z}_w^{-1} & \tilde{\mathbf{S}}_C^{++}(-kH) \\ \tilde{\mathbf{S}}_C^{--}(kH) & \mathbf{Z}_w^{-1} \end{bmatrix}^{-1}, \quad (27)$$

describes scattering of the Cartesian flow components from the walls. The 3×3 matrices \mathbf{Z}_w represent scattering of the flow from a single wall, and the matrices $\tilde{\mathbf{S}}_C^{++}(-kH)$ and $\tilde{\mathbf{S}}_C^{--}(kH)$ show the propagation of the flow field between the walls during the multiple-reflection process. The structure of the expressions (23)–(27) is schematically represented in Fig. 1. The explicit expressions for the component matrices (24)–(27) are listed in Appendix D.

We note that due to symmetries of the transformation and displacement matrices and the symmetry

$$\tilde{\mathbf{Z}}_{\text{TW}}(\mathbf{k}) = [\tilde{\mathbf{Z}}_{\text{TW}}(\mathbf{k})]^\dagger \quad (28)$$

of the two-wall scattering matrix, the Lorentz symmetry of the two-wall Green's matrix (23) is explicit.

E. Far-field asymptotic form

The exact Cartesian representation (23)–(27) of the wall contribution to the Green's matrix G'_{ij} involves a two-dimensional Fourier integral, which has to be evaluated numerically. However, for sufficiently large interparticle separations the calculation can be greatly simplified by using the far-field asymptotic expressions derived in [29]. Below we summarize this result.

The derivation of the asymptotic expressions for the Green's matrix

$$G_{ij} = G_{ij}^0 + G'_{ij} \quad (29)$$

relies on the observation that for large lateral interparticle distances, $\rho_{12} \gg H$, the disturbance flow scattered from the particles assumes the Hele–Shaw (i.e., lubrication) form. Accordingly, the far-field disturbance flow \mathbf{v}^{as} is driven by a two-dimensional harmonic pressure field p^{as} ,

$$\mathbf{v}^{\text{as}} = -\frac{1}{2}\eta^{-1}z(H-z)\nabla_{\parallel} p^{\text{as}}. \quad (30)$$

The pressure p^{as} is independent of the vertical variable z and satisfies the two-dimensional Laplace's equation

$$\nabla_{\parallel}^2 p^{\text{as}}(\boldsymbol{\rho}) = 0, \quad (31)$$

where $\boldsymbol{\rho} = (x, y)$ is the lateral position with respect to the particle, and ∇_{\parallel} is the two-dimensional gradient operator with respect to the lateral coordinates. The result (30) can be obtained using a lubrication expansion of the Stokes equations in the small parameter H/ρ (where $\rho = |\boldsymbol{\rho}|$).

To obtain the asymptotic expression for the Green's matrix G_{ij} we use the results listed in Appendices A and B. Accordingly, the asymptotic flow produced by a force multipole (B3) centered at the position of particle j is expressed in terms of the Hele–Shaw basis (A1) using relation (B2). The resulting Hele–Shaw multipolar flow is translated to the position of particle i using the displacement formula (A3). Finally the Hele–Shaw field is transformed back into the spherical basis using relation (B1). The above procedure [29] yields a compact expression of the form

$$G_{ij}^{\text{as}}(lm\sigma | l'm'\sigma') = -\frac{6}{\pi\eta H^3} C(Z_i; lm\sigma) S_{\text{cyl}}^{+-}(\boldsymbol{\rho}_{ij}; m | m') C(Z_j; l'm'\sigma'), \quad (32)$$

where the component matrices C and S_{cyl}^{+-} are given by Eqs. (A4) and (B4)–(B7). As explained in [29], the correction

$$\delta G_{ij} = G_{ij} - G_{ij}^{\text{as}} \quad (33)$$

to the asymptotic result (32) decays exponentially with

the lateral interparticle distance ρ_{ij} on the lengthscale H . Typically, the asymptotic approximation $G_{ij} \approx G_{ij}^{\text{as}}$ yields accurate results for $\rho_{ij}/H \gtrsim 2$.

Z/a	d/H						
	0.999	0.995	0.990	0.950	0.900	0.500	0.200
1.1					0.641	0.583	0.286
1.01			0.418	0.498	0.520	0.401	0.188
1.007			0.415	0.483	0.502	0.382	0.179
1.005		0.376	0.409	0.469	0.486	0.366	0.171
1.001	0.304	0.350	0.368	0.409	0.419	0.306	0.141

TABLE I: Normalized translational velocity U_x/U_p of a single sphere of diameter $d = 2a$ in imposed parabolic flow (1), for different wall separations H and particle positions Z with respect to the lower wall.

Z/a	d/H						
	0.999	0.995	0.990	0.950	0.900	0.500	0.200
1.1					0.0197	0.723	1.189
1.01			5.14E-4	0.101	0.177	0.620	0.903
1.007			0.0159	0.109	0.181	0.600	0.866
1.005		1.95E-4	0.0269	0.115	0.184	0.582	0.834
1.001	2.34E-5	0.0362	0.0556	0.127	0.183	0.504	0.705

TABLE II: Normalized angular velocity $H\Omega_y/U_p$ of a single sphere of diameter $d = 2a$ in imposed parabolic flow (1), for different wall separations H and particle positions Z with respect to the lower wall.

F. Numerical implementation

In order to determine the resistance matrices (21) and (22), the induced-force-multipole equation (18) is solved with the matrix (19) evaluated using known results [32, 38] for Z_i^{-1} and G_{ij}^0 , and our Cartesian representation (23) for G'_{ij} . For sufficiently large interparticle distances a simpler relation (32) may be used instead. After the friction matrices have been obtained, the mobility matrix (5) can be calculated from expressions (6) and (7).

To accelerate numerical convergence of the Fourier integral in (23) (especially, when both particles i and j are close to a single wall), the integrand (24) is decomposed into two single-wall contributions Ψ_L and Ψ_U and the correction term

$$\Psi(k) = \Psi_L(k) + \Psi_U(k) + \delta\Psi(k). \quad (34)$$

The single wall contributions can be integrated analytically [39, 40]. Moreover, as shown in [29], the correction term $\delta\Psi(k)$ is easier to integrate numerically than the original highly oscillatory integrand $\Psi(k)$.

As in other numerical algorithms based on a multipolar expansion of Stokes flow [39, 41] the force-multipole equation (18) is truncated at a given multipolar order $l = l_{\max}$ before it is solved numerically. To accelerate the convergence of the approximation with l_{\max} we employ the standard lubrication correction [42] on the friction-matrix level. We closely follow the implementation of the method described in [39] (for a single wall problem). Accordingly, the translational-rotational friction matrix $\zeta_{ij} = \zeta_{ij}^{AB}$ ($A, B = t, r$) is represented as a combination

$$\zeta_{ij} = \zeta_{ij}^{\text{sup},2} + \zeta_{ij}^{\text{sup},w} + \Delta\zeta_{ij}^* \quad (35)$$

of the two-particle superposition contribution in free space $\zeta_{ij}^{\text{sup},2}$, the single-particle/single-wall superposition contribution $\zeta_{ij}^{\text{sup},w}$, and the remainder $\Delta\zeta_{ij}^*$. The superposition contributions $\zeta_{ij}^{\text{sup},2}$ and $\zeta_{ij}^{\text{sup},w}$ are determined very accurately using the power-series expansions of the friction matrix in the inverse interparticle separation and the inverse distance between the particle and wall, respectively. The remainder $\Delta\zeta_{ij}^*$, evaluated as a difference between the multipolar expansion of the full friction matrix and the superposition contributions, converges with l_{\max} much faster than the full friction matrix ζ_{ij} itself.

In the present implementation of our method, the linear equation (19) is solved by matrix inversion. Thus, the numerical cost of the calculation scales as $O(N^3)$ with the number of particles N . (Numerical cost of this order is typical of unaccelerated Stokesian-dynamics algorithms.) We note, however, that the PPPM or fast-multipole acceleration techniques [43] can naturally be used in our Cartesian-representation algorithm—we will return to this problem in our future publications.

IV. RESULTS AND DISCUSSIONS

We now present some characteristic examples of single- and many-particle results. We consider both the motion of freely suspended particles in the external flow (1) and forces and torques on fixed particles subjected to this flow. The results for an isolated particle are obtained with the truncation at the multipolar order $l_{\max} = 32$, which yields accuracy better than 0.1%. For two-particle and multi-particle systems we use $l_{\max} = 12$ and $l_{\max} = 8$, respectively. The corresponding accuracy

is of the order of 1 %.

A. Single particle system

Motion of a single particle in a parabolic flow between two planar walls was recently considered by Staben *et al.* [30] and by Jones [28] (see also much earlier results by Ganatos *et al.* [44]). We thus give here only limited results for this system. In Tables I and II we list a set of our highly accurate results for the linear and angular velocities (5) of a force- and torque-free particle in the parabolic flow (1). The linear velocity \mathbf{U} is normalized by the magnitude of the parabolic flow U_p , and the angular velocity $\mathbf{\Omega}$ by U_p/H . Only the x component of the linear velocity and the y component of the angular velocity are given because all the other components vanish by symmetry.

In order to verify our results and test the accuracy of the calculations reported in [30], the velocities U^x and Ω^y are given for a subset of configurations represented in Tables I and II of [30]. We also present some additional results for tight configurations with $H \approx d$.

We find that our results are in good agreement (up to three digits) with those reported in [30] for $Z/a \gtrsim 1.01$, where Z is the position of the particle center measured from the lower wall. For smaller gaps between the wall and the particle the discrepancies are about 1.5%. An exception is the rotational velocity in the tightest configuration reported in [30] (i.e., $d/H = 0.95$ and $Z/a = 1.007$), where the error is 11%. We expect that these discrepancies stem from inaccuracies of the boundary-integral calculations in [30]—the convergence tests we have performed indicate that the accuracy of our results is better than 0.05%. We also note that our results agree with those of Jones [28] and with our earlier results of a multiple-reflection method [45].

B. Two-particle system

1. Particle velocities

A sample of characteristic results for the translational and rotational velocities \mathbf{U}_i and $\mathbf{\Omega}_i$ ($i=1,2$) of two force- and torque-free particles in the parabolic flow (1) are presented in figures 2–5. The linear and angular velocities are normalized in these plots by U_p and U_p/d , respectively. The results are plotted versus the lateral particle distance ρ_{12}/H for a moderate channel width

$$H = 2d. \quad (36)$$

In Figs. 2 and 4 the particle 1 is in the center position $Z_1 = H/2$, and in Fig. 3 and 5 it is in the off-center position $Z_1 = H/3$. The results are given for several vertical positions Z_2 of particle 2. (We recall that Z_i denotes the distance of particle (i) from the lower wall.) In Figs. 2

and 3 the particle pair is oriented in the longitudinal direction x and in Figs. 4 and 5 in the transverse direction y with respect to the flow. We note that $U_y = \Omega_x = \Omega_z = 0$ for the longitudinal configuration and $U_y = U_z = \Omega_x = 0$ for the transverse configuration, by symmetry.

The results in Figs. 2–5 indicate that the effect of mutual particle interactions is small if both particles are at the same vertical position in the channel. The effect is the largest if one of the particles is near the channel center and the other close to a wall. The results also reveal a different behavior in the near-field and far field regions, as discussed below.

a. Near-contact and intermediate region The results in Figs. 2–5 indicate that the dependence of the linear and rotational particle velocities on the interparticle distance is much more complicated in the wall-bounded system than in free space. This complex behavior stems from the competition between the tangential and normal lubrication forces and backflow effects associated with the velocity field scattered from the walls.

For near-contact particle configurations

$$\epsilon_{12} \ll 1 \quad (37)$$

(where $\epsilon_{12} = R_{12}/d - 1$ is the dimensionless gap between the particle surfaces, and $R_{12} = |\mathbf{R}_1 - \mathbf{R}_2|$) the particle dynamics is strongly influenced by the lubrication forces. The normal relative particle motion is arrested by the $O(\epsilon_{12}^{-1})$ normal lubrication force at the dimensionless gap ϵ_{12} of several percent. The relative tangential and rolling motions are opposed by much weaker $O(\log \epsilon_{12})$ lubrication forces. These motions are thus still quite substantial for $\epsilon_{12} \approx 10^{-3}$ and vanish only for nonphysically small gaps.

A decrease in the relative tangential and rotational particle motion at small interparticle distances results in an increased overall dissipation, which may cause a decrease of the horizontal particle velocities even in symmetric particle configurations with $Z_2 = Z_1$ or $Z_2 = H - Z_1$ (cf., the results for $Z_1/H = \frac{1}{3}$ and $Z_2/H = \frac{1}{3}, \frac{2}{3}$ in Fig. 3). We note that a pair of touching particles in a transverse configuration (Figs. 4 and 5) does not move, in general, as a rigid body, because there is no lubrication resistance to the relative particle rotation around the axis connecting their centers.

In some cases the normal and tangential lubrication forces have an opposite effect on a given velocity component. This produces sharp kinks in some curves at near-contact positions (e.g., U_{1z} and U_{2z} for $Z_2 = 2.67a$ in Fig. 3). An additional change of sign of particle velocities relative to the velocities at infinite interparticle separations $\rho_{12} \rightarrow \infty$ may occur due to a backflow associated with scattering of the flow from the walls. Due to a combination of the lubrication and back-flow effects, the z component of the particle velocities changes sign twice for some longitudinal configurations.

b. Far-field region As discussed in Sec. III E, for large lateral interparticle distances, the hydrodynamic interactions in a wall-bounded system are determined

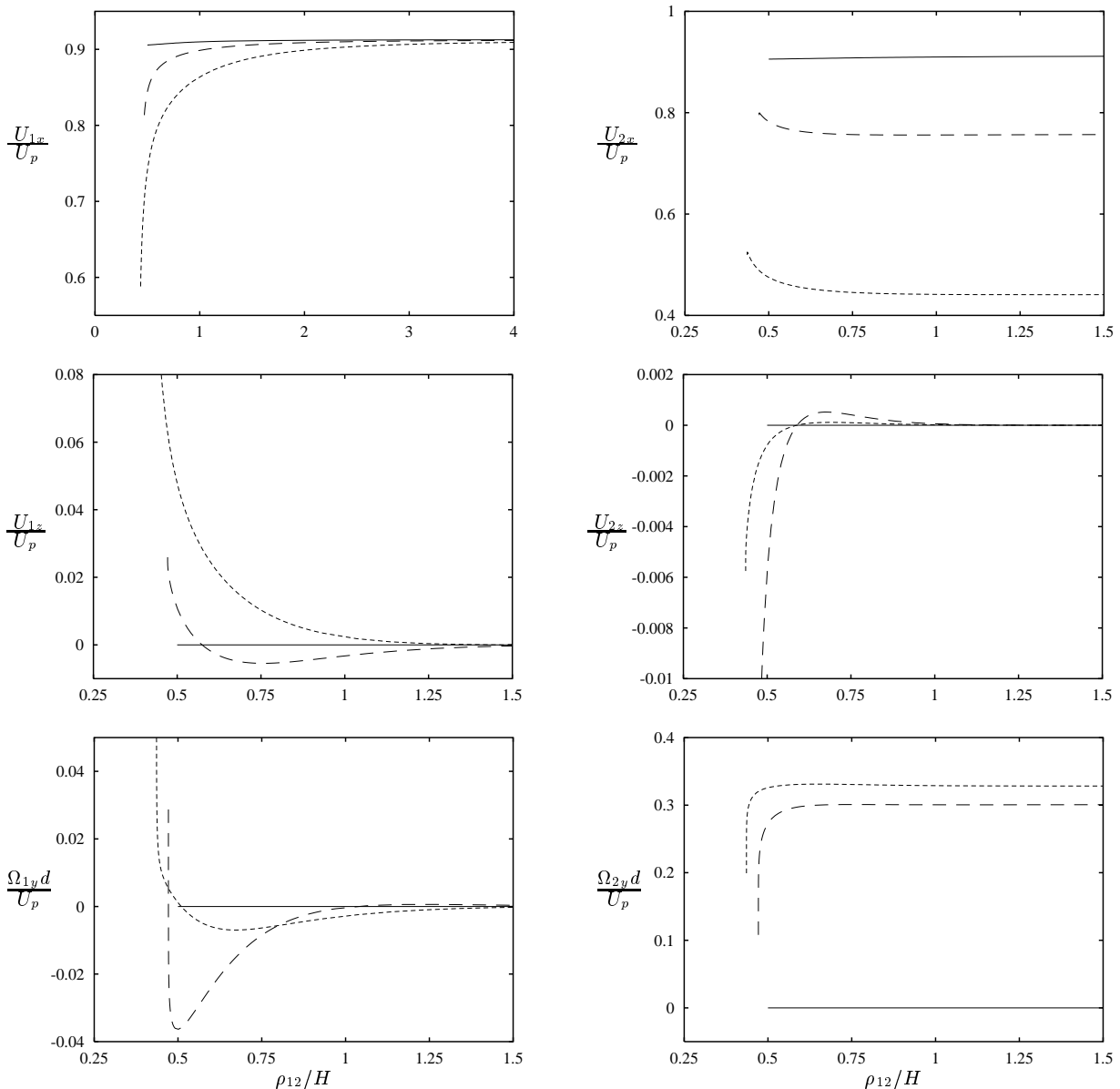


FIG. 2: Normalized linear and angular velocities of two spheres of diameter $d = 2a$ in imposed parabolic flow (1), versus particle lateral distance ρ_{12} normalized by wall separation H . The particle pair has the longitudinal orientation with respect to the flow direction, the wall separation is $H = 2d$, and sphere 1 is in the center position $Z_1 = 2a$. The positions of sphere 2 are $Z_2 = 1.02a$ (short-dashed line), $Z_2 = 1.33a$ (long-dashed line), $Z_2 = 2.0a$ (solid line).

by the far-field form of the disturbance flow scattered from the particles. The scattered flow has the Hele–Shaw form described by Eqs. (30) and (31). We recall that the asymptotic form of the flow field is approached exponentially on the lengthscale H .

Taking into account the symmetry of the problem we find that the far-field disturbance velocity produced by a particle in external flow (1) is given by equation (30)

with the pressure of the form

$$p^{\text{as}} \sim \frac{\cos \phi}{\rho}, \quad (38)$$

where ϕ is the polar angle between the lateral position vector $\boldsymbol{\rho}$ and the flow direction $\hat{\mathbf{e}}_x$. To the leading order in the multiple scattering expansion, relations (30) and (38) determine thus the far-field form of the hydrodynamic resistance and mobility functions for a pair of particles in the external parabolic flow.

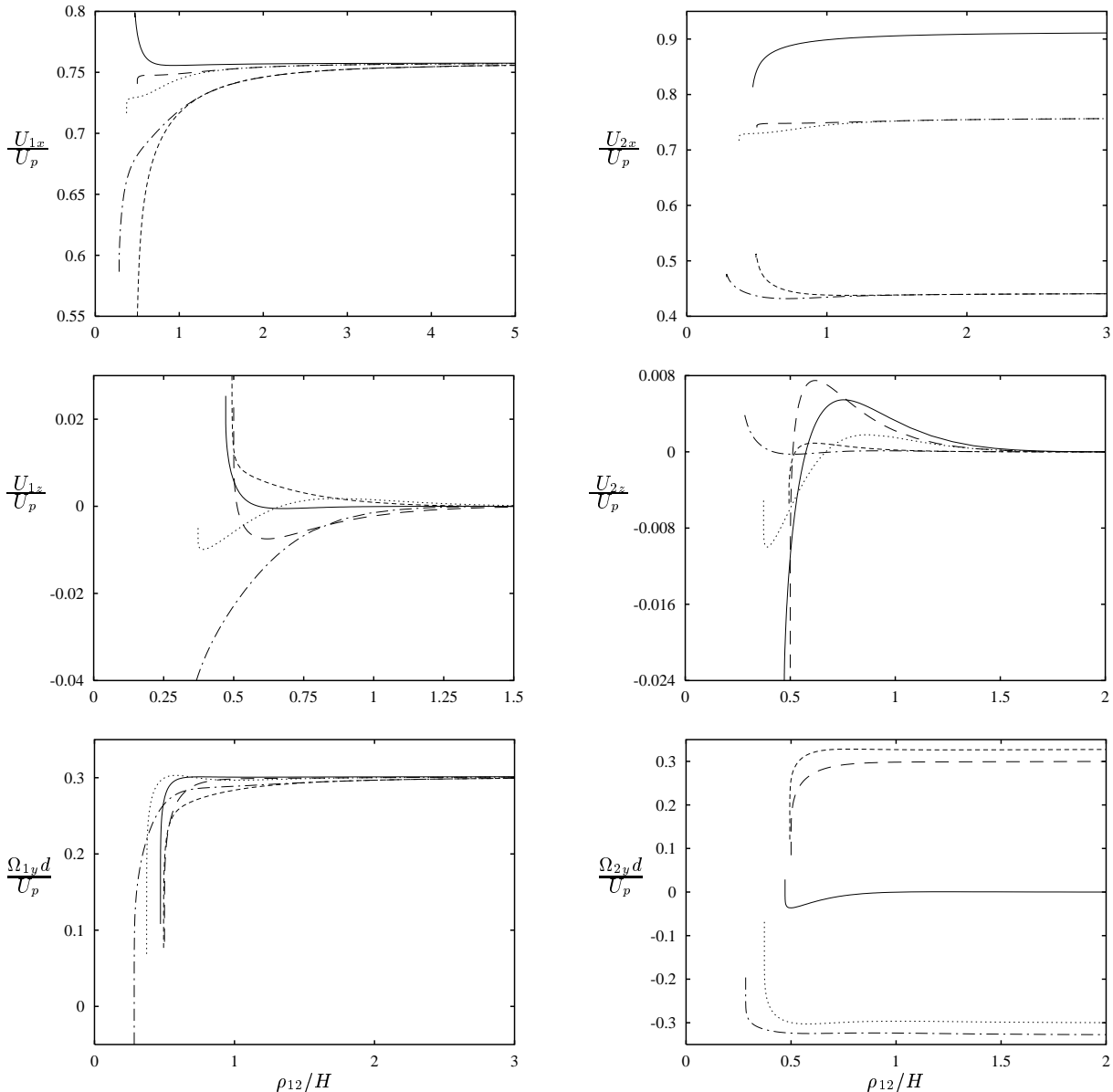


FIG. 3: Same as figure 2 except that particle 1 is in an off-center position $Z_1 = 1.33a$, and the positions of particle 2 are $Z_2 = 1.02a$ (short-dashed line), $Z_2 = 1.33a$ (long-dashed line), $Z_2 = 2.0a$ (solid line), $Z_2 = 2.67a$ (dotted line), $Z_2 = 2.98a$ (dash-dot line).

In particular, Eqs. (30) and (38) indicate that the flow \mathbf{v}^{as} has only lateral components. It follows that the z components of the translational and rotational particle velocities (4) vanish in the far-field regime. This behavior is clearly seen in Figs. 2–5, where these velocity components approach zero exponentially.

Next, the disturbance field (30) with the pressure given by Eq. (38) behaves as

$$v^{\text{as}} \sim \frac{1}{\rho^2}. \quad (39)$$

Thus the linear and angular lateral velocities shown in

Figs. 2–5 approach the one-particle asymptotic values as $O(\rho^{-2})$. The result (39) should be contrasted with the behavior

$$v^{\text{as}} \sim \frac{1}{\rho} \quad (40)$$

in free space and

$$v^{\text{as}} \sim \frac{1}{\rho^3} \quad (41)$$

in the presence of a single wall (where we assume that $Z_1, Z_2 \ll \rho$). According to Eqs. (39)–(41), the decay

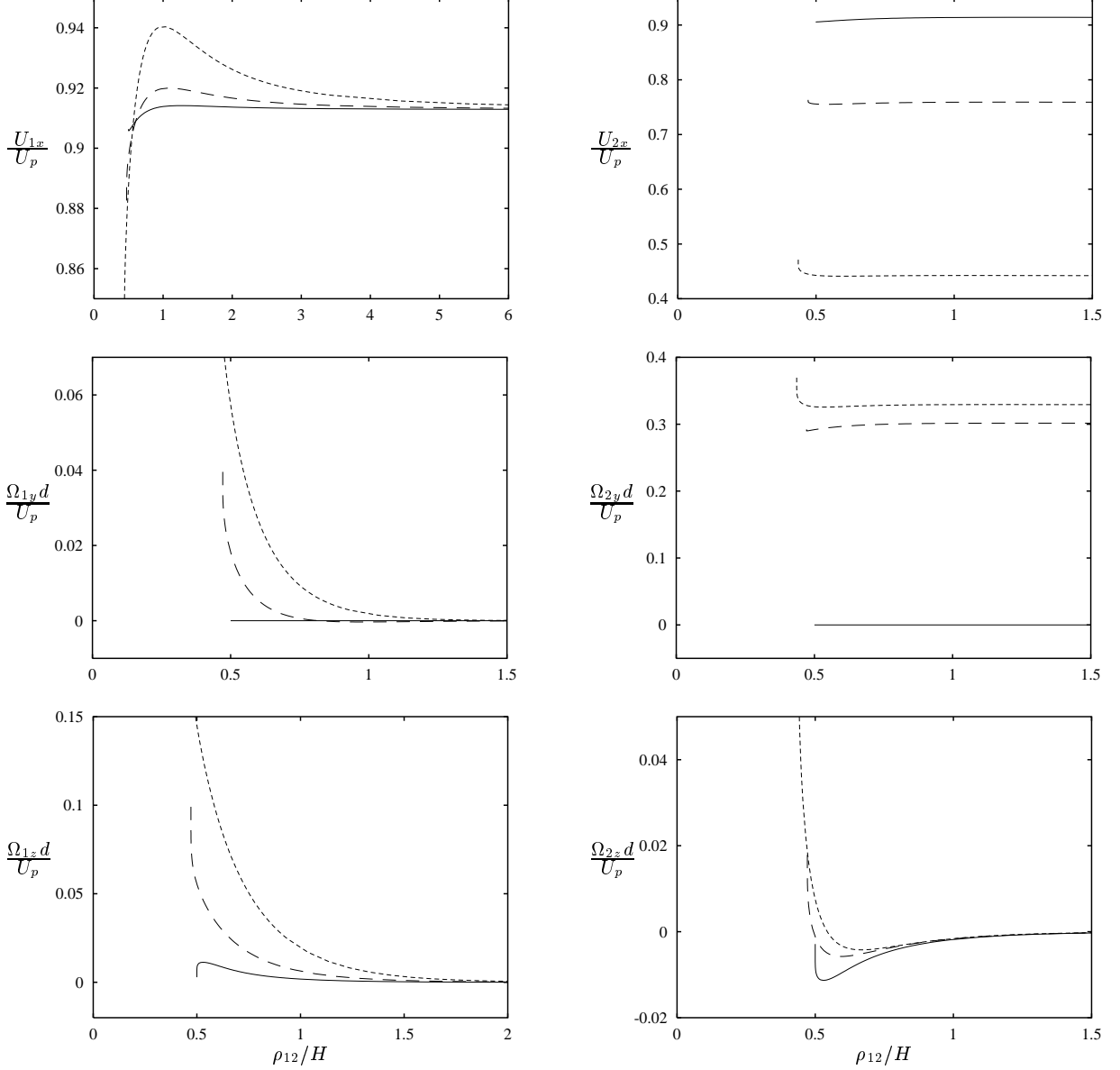


FIG. 4: Same as figure 2 except that for the transverse orientation of the particle pair.

of the far-field flow in the presence of one or two walls is faster than the corresponding decay in free space, because the walls absorb momentum, and thus they slow the fluid down.

On the other hand, the decay of the flow field (39) in the two-wall system is slower than the decay (41) in the presence of a single wall. This behavior stems from fluid-volume conservation constraint. In the system confined by a single wall the fluid displaced by the particle primarily flows above the particle, far from the wall, where it encounters small resistance. In contrast, in the presence of two walls, the flow is limited to the quasi-two-dimensional region; hence, it has a longer range.

Since the total flux associated with the quasi-two-dimensional flow (39) vanishes for $\rho \rightarrow \infty$, the fluid velocity must form a backflow pattern, unlike the behavior in the unbounded three-dimensional space. The backflow, described by the dipolar velocity field (30) and (38), results in an enhancement of relative particle motion for the transverse orientation of the particle pair (as seen for some particle configurations in the top panels of Figs. 4 and 5). We note that an analogous behavior was discussed by Cui *et al.* [19] in their study of pair diffusion in a confined, quasi-two-dimensional colloidal suspension. Similar effect was also independently described in our recent papers [26, 27].

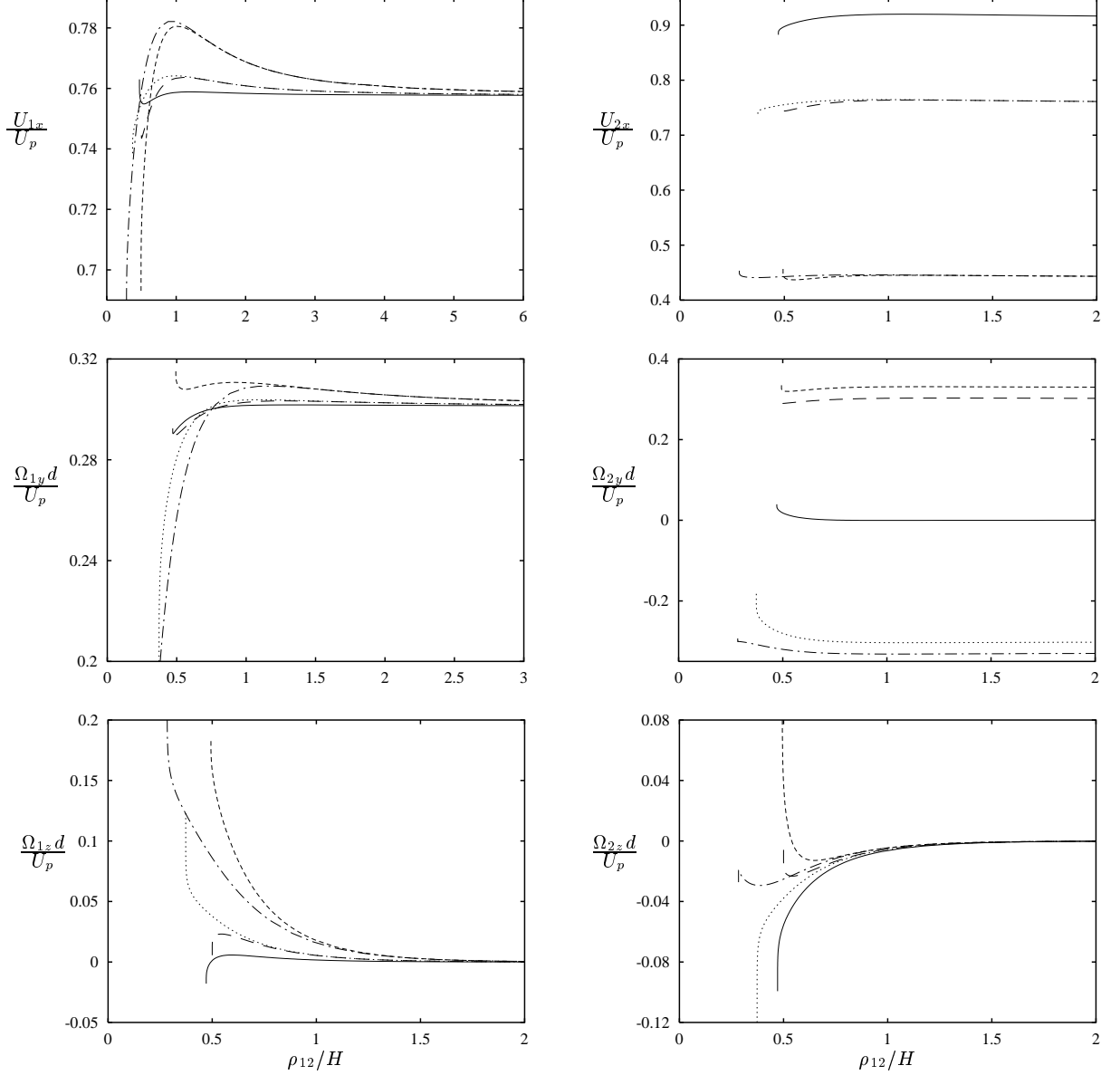


FIG. 5: Same as figure 3 except that for the transverse orientation of the particle pair.

2. Crossover behavior

The far-field disturbance flow, discussed above, affects not only the velocities of freely suspended particles, but also the hydrodynamic resistance force (3) acting on immobile particles in the external flow (1). Figures 6 and 7 illustrate the crossover of the resistance force between the three regimes corresponding to the disturbance flows of the form given by equations (39)–(41). To emphasize the behavior of the force in the far-field regime, the results are shown for the x component, $\delta\bar{F}_{ix}$, of the rescaled

force perturbation

$$\delta\bar{\mathbf{F}}_i = \left(\frac{\rho_{12}}{d}\right)^2 \delta\mathbf{F}_i, \quad (42)$$

where

$$\delta\mathbf{F}_i = (\mathcal{F}_i - \mathcal{F}_i^\infty)/F_{\text{st}}, \quad (43)$$

with $F_{\text{st}} = 3\pi\eta d$ denoting the Stokes resistance force, and \mathcal{F}_i^∞ representing the value of the force \mathcal{F}_i for $\rho_{12} \rightarrow \infty$.

In Figs. 6 and 7 force perturbation $\delta\bar{F}_{ix}$ is plotted versus the lateral particle separation ρ_{12} for two particles at the same vertical position $Z_1 = Z_2$. In one configuration,

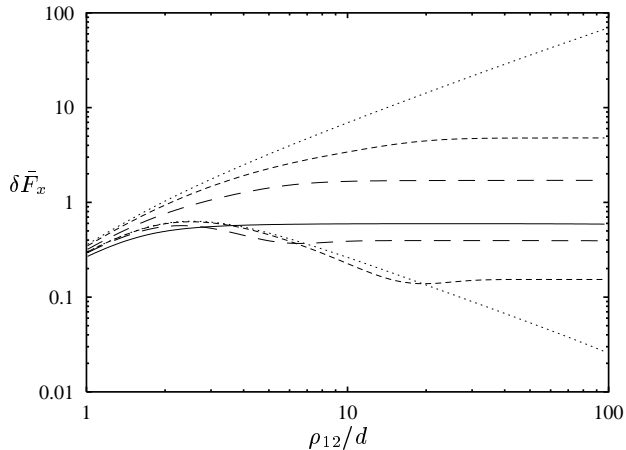


FIG. 6: Rescaled force perturbation (42) versus interparticle distance ρ_{12} normalized by the particle diameter d for a pair of particles in longitudinal orientation. Wall separation $H = 1.02d$ (solid line), $H = 5d$ (long-dashed lines), $H = 16d$ (short-dashed lines), $H = \infty$ (dotted lines). The top three lines correspond to particles in the center plane $Z_1 = Z_2 = \frac{1}{2}H$, and the bottom three to particles in the near-wall configuration $Z_1 = Z_2 = 1.02a$. For $H = 1.02d$ (middle line) the center and near-wall configurations coincide.

the particles are at the center plane

$$Z_1 = Z_2 = \frac{1}{2}H, \quad (44)$$

and in the other one they are close to the lower wall,

$$Z_1 = Z_2 = 1.02a. \quad (45)$$

The results are shown for several different wall separations. Since the particles are at the same vertical position, the force $\delta \bar{F}_x \equiv \delta \bar{F}_{ix}$ is independent of the particle index i . Figure 6 represents the results for the longitudinal orientation of the particle pair, $\boldsymbol{\rho}_{12} = \rho_{12}\hat{\mathbf{e}}_x$, and Fig. 7 the results for the transverse orientation $\boldsymbol{\rho}_{12} = \rho_{12}\hat{\mathbf{e}}_y$. The force perturbation (42) for the longitudinal orientation is positive. It is shown on the logarithmic scale to emphasize the algebraic asymptotic behavior. For the transverse orientation the perturbation force in the wall-bounded systems changes sign due to the backflow effects discussed in Sec. IV B 1. The results are thus plotted on a linear scale in two separate panels for the center (top panel) and the near-wall (bottom panel) configurations.

The results shown in Figs. 6 and 7 clearly demonstrate the crossover between different regimes corresponding to the far-field disturbance velocity fields of the form (39)–(41). For very large wall separations $H \rightarrow \infty$ and the center particle position (44) the rescaled force perturbation (42) behaves as $\delta \bar{F}_x \sim \rho_{12}$, which indicates that $\delta F_x = O(\rho_{12}^{-1})$, in agreement with the estimate (40) of the disturbance-flow magnitude in free space. For the near-wall position (45) and the longitudinal orientation

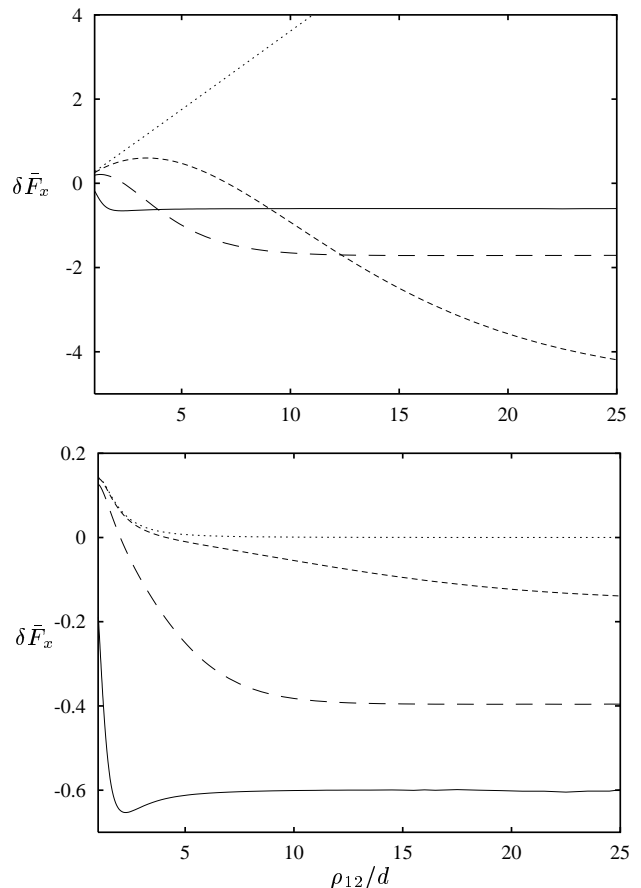


FIG. 7: Same as Fig. 6, except that for the transverse orientation of the particle pair. The top panel corresponds to particles in the center plane $Z_1 = Z_2 = \frac{1}{2}H$, and the bottom panel to particles in the near-wall configuration $Z_1 = Z_2 = 1.02a$.

of the particle pair we find $\delta F_x = O(\rho_{12}^{-3})$, consistently with the estimate (41). In contrast, $\delta F_x = O(\rho_{12}^{-5})$ in the transverse case, due to an additional cancellation of the far-field contributions.

For finite wall separations the force perturbation crosses over from the above-described behavior in the regime $a \ll \rho_{12} \ll H$ to the behavior $\delta F_x = O(\rho_{12}^{-2})$ (i.e., $\delta \bar{F}_x \sim \text{const}$) for $\rho_{12} \gg H$, in agreement with Eq. (39). Typically, the far-field behavior $O(\rho_{12}^{-2})$ is observed already for $\rho_{12} \gtrsim 2H$.

C. Multiparticle systems

In this section we examine the influence of the walls on the hydrodynamic interactions in confined multi-particle systems. We focus on collective phenomena that involve cumulative effects of the far-field flow (39). As shown in our recent studies of particle motion in quiescent fluid [26, 27, 29], the backflow associated with the dipolar

form (30) and (38) of the far-field velocity may produce a strong, positive feedback resulting in large magnitudes of induced forces. In such cases the far-field flow dominates the behavior of the system. Below we examine similar phenomena for particles in the imposed parabolic flow.

1. Motion of linear arrays of spheres

First we analyze the effect of confinement on the motion of rigid linear arrays of touching spheres. In earlier papers [26, 27, 29], we have shown that the behavior of such arrays in quiescent fluid is strongly affected by the walls. In particular we have demonstrated that, unlike in free space, the hydrodynamic resistance force in channels with $H \approx d$ depends significantly on the orientation of the array with respect to its velocity. If the orientation of the array, moving along the channel, is parallel to the velocity, the resistance force evaluated per one sphere decreases with the length of the array. In contrast, for the transverse orientation the resistance force per particle increases nearly linearly with the array length. This increase results from the pressure buildup associated with the positive-feedback backflow effects.

The motion of linear arrays of spheres in the imposed parabolic flow (1) is illustrated in Fig. 8 and 9. The arrays are parallel to the walls and are oriented either in the longitudinal direction x or the transverse direction y . Figure 8 presents the translational velocity of arrays with different length, placed in the mid-plane $z = \frac{1}{2}H$. The results are given for several channel widths H . Figure 9 shows linear and angular velocities of arrays at different vertical positions in the channel. The linear velocities are non-dimensionalized by the local velocity of the imposed flow

$$v_0 = v^{\text{ext}}(Z) \quad (46)$$

and the angular velocities by the local shear rate

$$\gamma_0 = \frac{\partial v^{\text{ext}}(Z)}{\partial Z} \quad (47)$$

evaluated at the position Z of the array center. For the mid-plane position $z = \frac{1}{2}H$, v_0 is identical to the amplitude U_p of the imposed flow (1).

The results in Fig. 8 indicate that the normalized velocity of an array U_x/U_p is smaller in channels with smaller width. This behavior stems primarily from the increased dissipation in the gaps between the particles and the channel walls. The decrease of the mobility is strongest for long arrays in longitudinal orientation—the far-field disturbance flow produced by each of the particles opposes the motion of the array in this case. For the transverse orientation, the scattered flow acts in the direction of the external flow; due to the cooperative feedback effects longer arrays move faster than the shorter ones. In narrow channels with $H \approx d$, very long chains in transverse orientation translate with the velocity that is close to the average velocity of the unperturbed fluid.

A set of results for short ($N = 3$) and a long ($N = 20$) linear arrays at off-center positions in channels with different width is presented in Fig. 9. The configurations are parametrized by the normalized distances of the particle surfaces from the lower and upper walls,

$$\epsilon_L = \frac{1}{2}(Z - a)/a, \quad \epsilon_U = \frac{1}{2}(H - Z - a)/a. \quad (48)$$

The translational and rotational velocities are shown for arrays at two vertical positions $\epsilon_L = 0.001$ and $\epsilon_L = 1.1$, and they are plotted versus the distance ϵ_U .

The results in the upper panels of Fig. 9 indicate that the translational velocity of an array at a fixed distance from the lower wall diminishes rapidly with the decreasing $\epsilon_U \ll \epsilon_L$ due to the $O(\log \epsilon_U)$ lubrication resistance associated with the interaction with the upper wall. In the case of the longitudinal orientation of the chain, the translational and rotational velocities saturate at $\epsilon_U \approx 1$. In contrast, for the transverse orientation, the effect of the upper wall on the translational velocity of the array has a much longer range, especially for the larger value of the chain length N . Moreover, the effect of the upper wall is more pronounced for $\epsilon_L = 0.001$ than for $\epsilon = 0.1$. These observations are consistent with the backflow mechanisms discussed above.

Lower panels of Fig. 9 represent the normalized angular velocity Ω_y/γ_0 of the arrays. We note that the angular velocity itself changes sign for $\epsilon_L = \epsilon_U$; however, the normalized quantities shown in Fig. 9 are positive, due to the corresponding change of sign of the local shear rate (47). For the longitudinal orientation of the chain the angular velocity is several orders of magnitude smaller than the angular velocity in the transverse case. This strong effect can easily be explained in terms of particle-wall lubrication forces. The rotation of the chain oriented perpendicularly to the flow is governed by the $O(\log \epsilon_L)$ lubrication resistance. The rotation of the chain oriented parallel to the flow involves motion of individual particles towards the wall and away from it, and thus the lubrication forces are much stronger $O(\epsilon_L^{-1})$.

2. Hydrodynamic drag on adsorbed particles

In Figs. 10–12 the results are presented for the hydrodynamic friction forces and torques on individual particles in arrays of spheres adsorbed on one of the walls in a parallel-wall channel. Understanding of such forces is important in an analysis of the removal of colloidal particles from a wall by an applied flow [46]. Moreover, our results provide a further illustration of hydrodynamic phenomena associated with the far-field form of the disturbance velocity field produced by the particles.

Figures 10 and 11 show forces and torques acting on individual particles in closely packed arrays of touching spheres. Arrays that are loosely packed are considered in Fig. 12. The results are given for a single sphere, linear arrays of spheres, and hexagonal arrays of spheres. The horizontal components of the forces and torques are

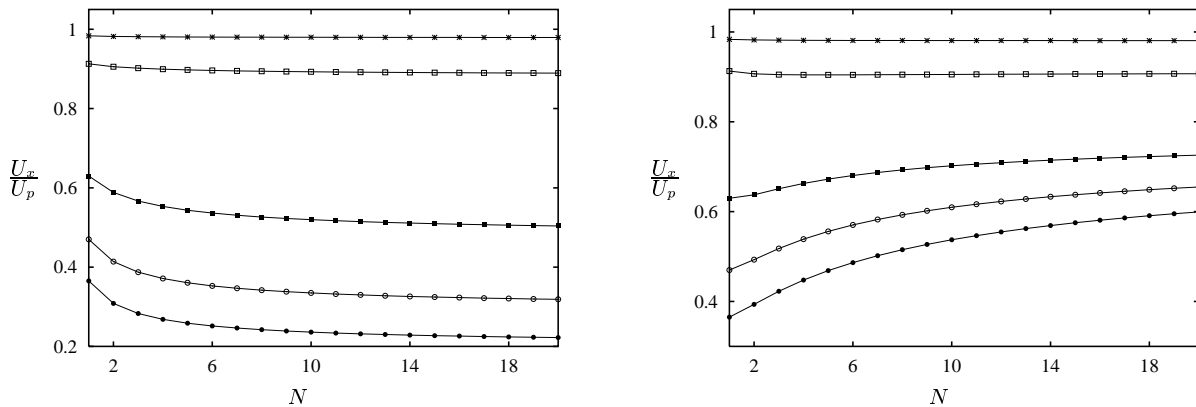


FIG. 8: Normalized translational velocity U_x/U_p of rigid, linear arrays of touching spheres, for the longitudinal (left panel) and transverse (right panel) orientation with respect to the imposed flow (1). The results are shown versus the number of particles in the array N . The arrays are in the center plane $z = \frac{1}{2}H$ between walls separated by $H = 1.004d$ (solid circles), $H = 1.02d$ (open circles), $H = 1.1d$ (solid squares), $H = 2.0d$ (open squares), $H = 4.5d$ (crosses).

represented by line segments and the normal components by the dashed (orientation away from the wall) and dotted (towards the wall) circles. The forces are scaled by $a\eta v_0$ and the torques by $a^2\eta v_0$, where v_0 is the local fluid velocity (46). The lengths of the line segments and the radii of the circles are proportional to the magnitude of the represented quantity.

The results presented in Fig. 10 indicate that the lateral drag force on a single particle only weakly depends on the channel width, while the forces on particles in linear arrays vary almost by a factor of five when the wall separation H changes from $2.02a$ to infinity. Similarly strong dependence of the forces on the channel width is observed for the two-dimensional arrays of spheres.

The hydrodynamic drag forces are the largest for linear arrays of spheres in narrow channels of the width only slightly bigger than the particle diameter (cf., the top panel of Fig. 10). The large forces are associated with the pressure buildup in front of the array [29]. As explained in Sec. IV C 1, the pressure buildup involves interaction of the flow with both walls in an essentially non-additive manner. Thus, as shown in [26], this effect is not captured by the usual approximation based on a superposition of two single-wall contributions.

The results for two-dimensional arrays of spheres involve significant screening effects resulting from mutual particle interactions. Accordingly, the lateral forces acting on individual spheres in two-dimensional arrays are smaller than in the corresponding linear-array systems. The forces on the first and last row of particles are larger than the forces on particles near the center of the array. This effect is most pronounced for large wall separations H —in narrow channels the relative force differences are smaller due to the quasi-two-dimensional character of the flow.

Our results for the vertical forces indicate that their magnitude is much smaller than the magnitude of the

lateral forces. Indeed, the only significant vertical forces exist on the first and last rows of particles in two-dimensional arrays. The maximal value of these forces occurs for $H \approx 4a$. When the channel width is smaller, the upper wall suppresses the vertical flow. On the other hand, when the gap between the top wall and the spheres is too large, the volume of fluid deflected by the array is distributed over the larger space, and the vertical flow becomes weaker. We note that there are no vertical forces on particles in linear arrays because of the flow-reversal symmetry.

The behavior of the torque exerted on the particles by the fluid is illustrated in Fig. 11. Characteristic features of the torque distribution can be explained using arguments similar to the ones given above. For example, the lateral torques are the largest for $H \approx 4a$, for the same reason as the corresponding behavior of the normal force. Our results indicate that the vertical component of the torque is significant only for particles at the edges of the arrays, especially for small values of H .

Figure 12 shows plots of forces on the spheres in loosely packed arrays of spheres. For linear arrays, the lateral forces are relatively small even for $H \approx 2a$ because the flow can pass through the inter-particle gaps without building up a substantial pressure drop. Moreover, the forces on particles in different positions in such arrays are of approximately equal magnitude. For the two-dimensional loosely packed arrays the lateral forces are larger than for the closely-packed case, which indicates that the screening effects are smaller.

V. CONCLUSIONS

We have used our recent Cartesian-representation algorithm to study hydrodynamic interactions of spherical particles in a parabolic flow between two parallel planar

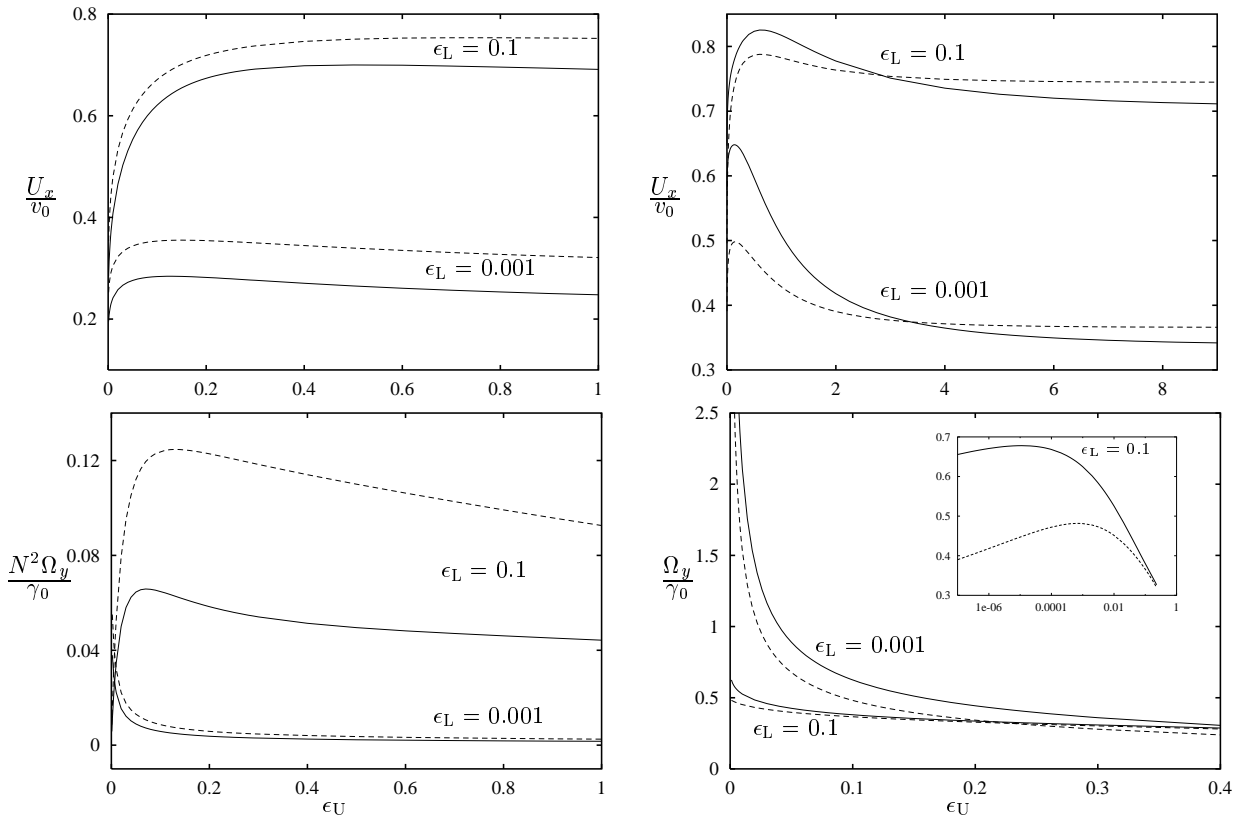


FIG. 9: Normalized translational and angular velocities of rigid, linear arrays of touching spheres with length $N = 3$ (dashed lines) and $N = 20$ (solid lines), for the longitudinal (left panel) and transverse (right panel) orientation with respect to the imposed flow (1). The distance (48) of the particle surfaces from the lower wall ϵ_L , as labeled; the results are shown versus the distance from the upper wall ϵ_U . The translational velocity U_x is normalized by the local fluid velocity (46); the angular velocity Ω_y is normalized by the local shear rate (47). For the longitudinal configuration the angular velocity is in additional rescaled by N^2 . The inset shows the region with small ϵ_U .

walls. An important feature of our method is that at each multipolar-approximation level the boundary conditions at the walls are exactly satisfied. This ensures that the far-field flow produced by the particles has a correct form of a two-dimensional Hele-Shaw lubrication velocity field. Our analysis indicates that the far-field flow and the associated backflow effects strongly affect hydrodynamic interactions in confined multiparticle systems.

We have presented a set of numerical results for a single particle, a pair of particles, and arrays of many particles. Our one-particle calculations agree well with earlier results [28, 30, 45]. For very tight configurations with small gaps between the particle surface and the walls we provide more accurate data than those reported previously [30]. For two-particle and multi-particle systems no accurate results have been available so far.

Our numerical calculations reveal that the pair and multiparticle hydrodynamic interactions in the wall bounded system are much more complex than the interactions in free space. In particular, unlike in free space, the sign of mutual friction and mobility functions

depends on the relative particle position in the flow-vorticity plane. The changes of sign result from combined effects of the short-range dissipation in the near-contact regions and backflow due to the confinement. Related backflow phenomena were recently observed in quasi-two-dimensional suspensions of Brownian particles [19]. For elongated particles in narrow slit pores, such a backflow results in a strongly non-isotropic diffusion constant [26, 27, 29, 47].

The far-field flow also determines the fluid velocity distribution and the hydrodynamic drag forces in two-dimensional arrays of particles adsorbed on a wall. Our results indicate that in narrow channels with the width H similar to the particle diameter d the hydrodynamic forces act mostly in the horizontal direction. Normal forces, which may lead to particle resuspension, are maximal in channels with $H \approx 2d$. Our results on hydrodynamic drag on immobile adsorbed particles can be used in an analysis of particle removal from a channel by a flow.

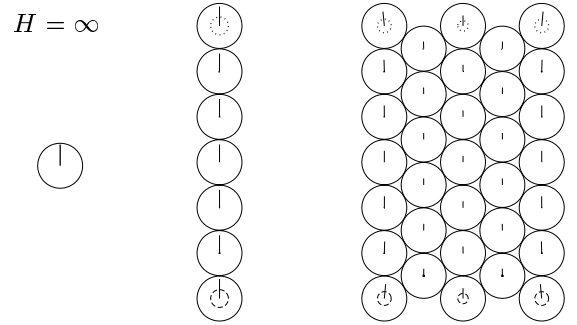
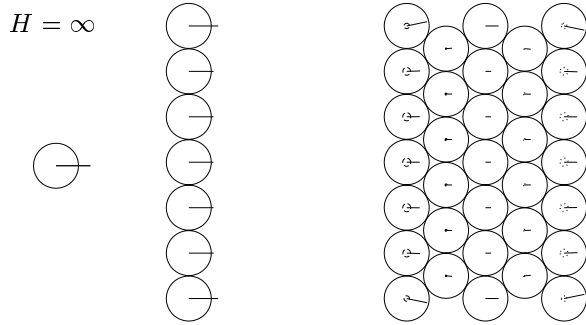
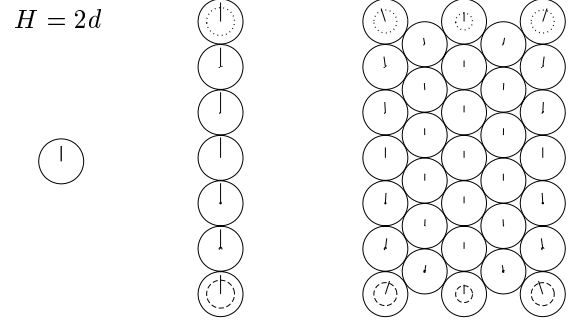
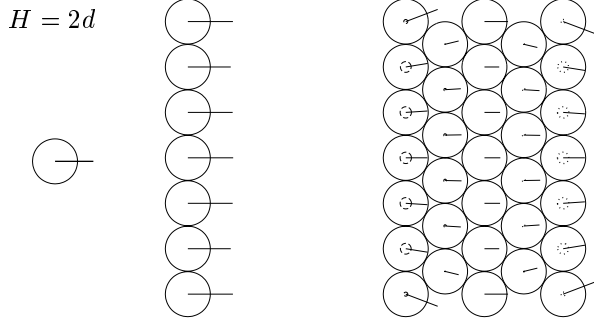
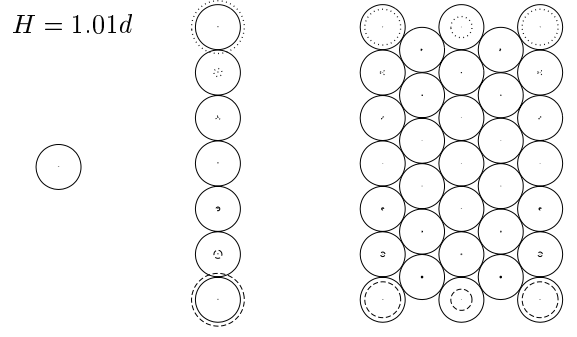
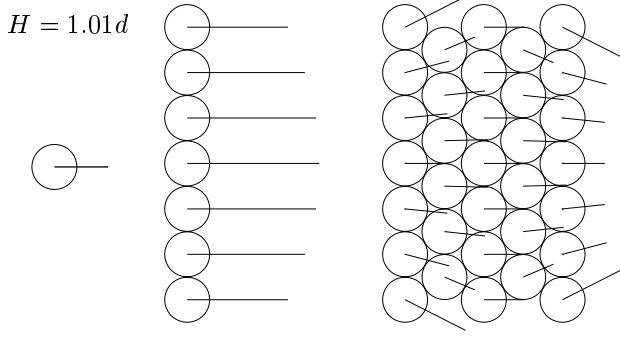


FIG. 10: Hydrodynamic drag forces on a single sphere and on individual particles in linear and hexagonal arrays of spheres adsorbed on a wall in a channel with the width H (as labeled). The spheres are depicted by solid circles. The lateral forces are represented by the line segments, and the normal forces by dashed (force away from the wall) or dotted (towards the wall) circles. A line segment (circle) of the length (radius) equal to the particle radius a represents a force of magnitude $20\pi a \eta v_0$, where v_0 is the local fluid velocity (46).

FIG. 11: Same as Fig. 10, except that the results are for the hydrodynamic torque. A line segment (circle) of the length (radius) equal to the particle radius a represents a torque of magnitude $8\pi a^2 \eta v_0$.

035 22. J. B. was supported by NSF grant cts-s0348175.

Acknowledgments

S. B. would like to acknowledge the support by NSF grant CTS-0201131. E. W. was supported by NASA grant NAG3-2704 and, in part, by KBN grant No. 5T07C

APPENDIX A: HELE-SHAW BASIS

As shown in [29], the far field-flow in the two-wall geometry has the Hele-Shaw, lubrication form. Such a flow can be represented in terms of singular (–) and non-

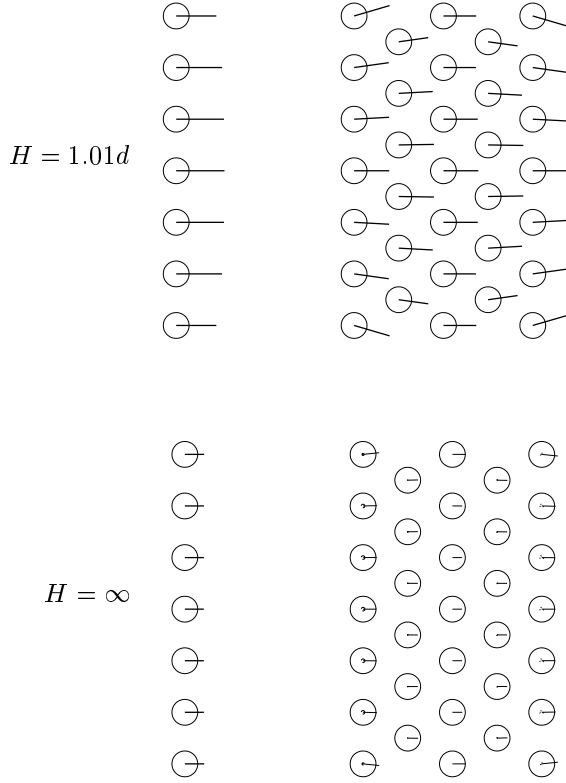


FIG. 12: Same as Fig. 10 except that the results are for loosely packed arrays of spheres.

singular (+) Hele–Shaw basis fields of the form

$$\mathbf{v}_m^{\text{as}+}(\mathbf{r}) = -\frac{1}{2}z(H-z)\nabla_{\parallel}\Phi_m^+(\boldsymbol{\rho}), \quad (\text{A1})$$

where

$$\Phi_0^-(\boldsymbol{\rho}) = -\ln \rho, \quad \Phi_m^-(\boldsymbol{\rho}) = \frac{1}{2|m|}\rho^{-|m|}e^{im\phi}, \quad m \neq 0 \quad (\text{A2a})$$

are singular and

$$\Phi_m^+(\boldsymbol{\rho}) = \rho^{|m|}e^{im\phi} \quad (\text{A2b})$$

non-singular two-dimension harmonic functions. Here $\boldsymbol{\rho}$ is the lateral position vector with the polar coordinates (ρ, ϕ) , and ∇_{\parallel} is the two-dimensional gradient operator with respect to the lateral coordinates.

The Hele–Shaw flow fields (A1) centered at lateral positions $\boldsymbol{\rho}_i$ and $\boldsymbol{\rho}_j$ are linked by the displacement formula

$$\mathbf{v}_{m'}^{\text{as}-}(\mathbf{r} - \boldsymbol{\rho}_j) = \sum_{m=-\infty}^{\infty} \mathbf{v}_m^{\text{as}+}(\mathbf{r} - \boldsymbol{\rho}_i) S_{\text{cyl}}^{+-}(\boldsymbol{\rho}_{ij}; m | m'), \quad (\text{A3})$$

where $\boldsymbol{\rho}_{ij} = \boldsymbol{\rho}_i - \boldsymbol{\rho}_j$. The term with $m = 0$ in the above relation vanishes because $\mathbf{v}_0^{\text{as}+} \equiv 0$ according to Eqs.

(A2b) and (A1). The prime at the summation sign is introduced to emphasize that this term is omitted.

The matrix

$$S_{\text{cyl}}^{+-}(\boldsymbol{\rho}; m | m') = \theta(-mm')(-1)^{m'} \frac{(|m| + |m'|)!}{|m|!|m'|!} \Phi_{m'-m}^-(\boldsymbol{\rho}) \quad (\text{A4})$$

in Eq. (A3) is identical to the displacement matrix for the two-dimensional harmonic potentials (A2). We note that due to the presence of the Heaviside step function

$$\theta(x) = \begin{cases} 0, & x < 0, \\ 1, & x \geq 0, \end{cases} \quad (\text{A5})$$

the Hele–Shaw basis fields with the same sign of indices $m, m' \neq 0$ do not couple in the displacement relation (A3).

APPENDIX B: TRANSFORMATION BETWEEN THE HELE–SHAW AND SPHERICAL BASIS SETS

In this Appendix we list some relations between the Hele–Shaw basis of asymptotic far field flows (A1) and the multipolar spherical basis fields defined in [32] (in the normalization introduced in [26]).

As shown in [26], the nonsingular Hele–Shaw field $\mathbf{v}_m^{\text{as}+}$ centered at the lateral position $\boldsymbol{\rho}_i$ has the following expansion in terms of non-singular spherical basis fields $\mathbf{v}_{lm\sigma}^+$ centered at $\mathbf{R}_i = \boldsymbol{\rho}_i + Z_i \hat{\mathbf{e}}_z$,

$$\mathbf{v}_m^{\text{as}+}(\mathbf{r} - \boldsymbol{\rho}_i) = \sum_{l\sigma} \mathbf{v}_{lm\sigma}^+(\mathbf{r} - \mathbf{R}_i) C(Z_i; lm\sigma). \quad (\text{B1})$$

There is also a reciprocal expression

$$\mathbf{u}_{lm\sigma}^{\text{as}}(\mathbf{r} - \boldsymbol{\rho}_j; Z_j) = -\frac{6}{\pi\eta H^3} \mathbf{v}_m^{\text{as}-}(\mathbf{r} - \boldsymbol{\rho}_j) C(Z_j; lm\sigma) \quad (\text{B2})$$

for the far-field flow $\mathbf{u}_{lm\sigma}^{\text{as}}$ produced, between the walls, by a force multipole

$$\mathbf{F}(\mathbf{r}) = a^{-2} \delta(r_j - a) \mathbf{w}_{lm\sigma}^+(\mathbf{r}_j) \quad (\text{B3})$$

(cf., the multipolar expansion (16)).

Explicit expressions for the transformation matrix $C(Z_i; lm\sigma)$ have been derived in [29]. Accordingly, the nonzero elements of $C(Z_i; lm\sigma)$ satisfy the condition

$$l + \sigma - |m| \leq 2, \quad (\text{B4})$$

and they can be written in the form

$$C(Z; l \pm \mu \sigma) = B_{l-\mu \sigma}^{\pm}(Z; \mu), \quad \mu = |m| \geq 1. \quad (\text{B5})$$

Here, the $B_{\lambda \sigma}^{\pm}(Z; \mu)$ are the elements of the 3×3 matrix

$$\{B_{\lambda\sigma}^{\pm}(Z; \mu)\}_{\lambda,\sigma=0,1,2} = \frac{1}{2}A^{\pm}(\mu) \begin{bmatrix} -Z(H-Z) & \mp(H-2Z) & 2 \\ \frac{-\mu(H-2Z)}{(\mu+1)(2\mu+3)^{1/2}} & \frac{\pm 2\mu}{(\mu+1)(2\mu+3)^{1/2}} & 0 \\ \frac{2\mu(\mu+1)^{1/2}}{(\mu+2)(2\mu+3)(\mu+5)^{1/2}} & 0 & 0 \end{bmatrix}, \quad (\text{B6})$$

with

$$A^{\pm}(\mu) = (\mp 2)^{\mu} \mu! \left[\frac{4\pi}{(2\mu+1)(2\mu)!} \right]^{1/2}. \quad (\text{B7})$$

The range $\lambda = 0, 1, 2$ of the index $\lambda = l - |m|$ in equation (B6) result from the conditions $|m| \leq l$ and (B4).

APPENDIX C: PROJECTION MATRIX Y

Relation (22) is derived by inserting expansion (17) of the external flow (1) into Eqs. (141) and (145) in Ref. [26]. Comparing Eqs. (3) and (22) to the resulting formula we conclude that the the matrix $Y_j(lm\sigma | p)$ is determined by the expansion

$$\mathbf{v}^{\text{ext}}(\mathbf{r}) = \sum_{lm\sigma} \mathbf{v}_{lm\sigma}^+(\mathbf{r} - \mathbf{R}_j) Y_j(lm\sigma | p) \quad (\text{C1})$$

of the parabolic flow (1) into the spherical basis centered at \mathbf{R}_j .

To obtain the explicit expression for the matrix $Y_j(lm\sigma | p)$, we represent the external parabolic flow (1) in terms of the Hele-Shaw asymptotic basis (A1),

$$\mathbf{v}^{\text{ext}} = -4U_p H^{-2} (\mathbf{v}_{-1}^{\text{as}+} + \mathbf{v}_1^{\text{as}+}). \quad (\text{C2})$$

Inserting expansion (B1) into the above relation and comparing the result to (C1) yields

$$Y_j(lm\sigma | p) = -4U_p H^{-2} (\delta_{m1} + \delta_{m-1}) C(Z_j; lm\sigma), \quad (\text{C3})$$

where δ_{mk} denotes the Kronecker delta. Using relations (B4)–(B7) for the matrix C we thus find

$$\{Y_j(\lambda+1 \pm 1 \sigma | p)\}_{\lambda,\sigma=0,1,2} = -4H^{-2} U_p \sqrt{\frac{2\pi}{3}} \begin{bmatrix} -Z_j(H-Z_j) & \mp(H-2Z_j) & 2 \\ \frac{-(H-2Z_j)}{2\sqrt{5}} & \frac{\pm 1}{\sqrt{5}} & 0 \\ \frac{2}{15\sqrt{3}} & 0 & 0 \end{bmatrix}. \quad (\text{C4})$$

All other elements of Y_j vanish, by Eq. (B4). [Sukalyan: verify !?.]

APPENDIX D: COMPONENT MATRICES IN CARTESIAN REPRESENTATION

In this Appendix we list explicit expressions for the component matrices in the Cartesian representation (23)–(27) of the Green's matrix \mathbf{G}'_{ij} . These expressions are derived in Ref. [26].

The component transformation matrices in Eq. (25)

can be represented in the factorized form

$$\mathbf{T}_{\text{CS}}^{\pm-}(\mathbf{k}, lm) = [\mathbf{T}_{\text{SC}}^{+\pm}(lm, \mathbf{k})]^{\dagger} = i^m (2\pi k)^{-1/2} e^{im\psi} \times \tilde{\mathbf{T}}_{\text{CS}}^{\pm-}(lm) \cdot \mathbf{K}(k, l), \quad (\text{D1})$$

where (k, ψ) are the polar coordinates of the vector \mathbf{k} . In the above expression

$$K(k, l; \sigma | \sigma') = \delta_{\sigma\sigma'} k^{l+\sigma-1}, \quad (\text{D2})$$

and

$$\tilde{\mathbf{T}}_{\text{CS}}^{\pm-} = (-1)^{l+m} \begin{bmatrix} c & -2b & 4a \\ b & -2a & 0 \\ a & 0 & 0 \end{bmatrix}, \quad (\text{D3a})$$

$$\tilde{\mathbb{T}}_{\text{CS}}^{--} = \begin{bmatrix} a & 0 & 0 \\ b & 2a & 0 \\ c & 2b & 4a \end{bmatrix}. \quad (\text{D3b})$$

The three independent scalar coefficients in equations (D3) are

$$a = [4(l-m)!(l+m)!(2l+1)]^{-1/2}, \quad (\text{D4a})$$

$$b = 2am/l, \quad (\text{D4b})$$

$$c = a \frac{l(2l^2 - 2l - 1) - 2m^2(l-2)}{l(2l-1)}. \quad (\text{D4c})$$

The component displacement matrices in Eqs. (26) and (27) are given by the relation

$$\tilde{\mathbb{S}}_{\text{C}}^{++}(kZ) = [\tilde{\mathbb{S}}_{\text{C}}^{--}(-kZ)]^\dagger = \begin{bmatrix} 1 & 0 & 2kZ \\ 0 & 1 & 0 \\ 0 & 0 & 1 \end{bmatrix} \mathbf{e}^{kZ}. \quad (\text{D5})$$

For rigid walls with no-slip boundary conditions the single-wall reflection matrix in Eq. (27) has the form

$$\mathbb{Z}_{\text{w}} = \begin{bmatrix} 1 & 0 & 0 \\ 0 & 1 & 0 \\ 0 & 0 & 1 \end{bmatrix}. \quad (\text{D6})$$

For planar interfaces with other boundary conditions (e.g., a surfactant-covered fluid-fluid interface discussed in [48]) the scattering matrix is different from identity, and it may depend on the magnitude of the wave vector k . Explicit expressions for scattering matrices for such systems will be presented elsewhere.

-
- [1] H. Faxén, “Der widerstand gegen die bewegung einer starren kugel in einer zähen flüssigkeit die zwischen zwei parallelen ebenen wänden eingeschlossen ist,” *Ark. Matematik, Astronomi Fysik* **18**, 1–52 (1924).
- [2] D. C. Prieve, F. Luo, and F. Lanni, “Brownian-motion of a hydrosol particle in a colloidal force-field,” *Faraday Discuss. Chem. Soc.* **83**, 297 (1987).
- [3] J. Y. Walz and L. Suresh, “Study of the sedimentation of a single particle toward a flat plate,” *J. Chem. Phys.* **103**, 10714–725 (1995).
- [4] L. P. Faucheux and A. J. Libchaber, “Confined Brownian motion,” *Phys. Rev. E* **49**, 5158–63 (1994).
- [5] B. Lin, J. Yu, and S. A. Rice, “Direct measurements of constrained Brownian motion of an isolated sphere between two walls,” *Phys. Rev. E* **62**, 3909–19 (2000).
- [6] T. Palberg and R. Biehl, “Sheared colloidal crystals in confined geometry: a real space study on stationary structures under shear,” *Faraday Discuss.* **123**, 133–43 (2003).
- [7] J. C. Crocker, J. A. Matteo, A. D. Dinsmore, and A. G. Yodh, “Entropic attraction and repulsion in binary colloids probed with a line optical tweezer,” *Phys. Rev. Lett.* **82**, 4352–5 (1999).
- [8] G. M. Whitesides and A. D. Stroock, “Flexible methods for microfluidics,” *Phys. Today* **54**, 42–8 (2001).
- [9] G. Subramanian, V. N. Manoharan, J. D. Thorne, and D. J. Pine, “Ordered macroporous materials by colloidal assembly: A possible route to photonic bandgap materials,” *Adv. Mater.* **11**, 1261–1265 (1999).
- [10] E. W. Seelig, B. Tang, A. Yamilov, H. Cao, and R. P. H. Chang, “Self-assembled 3D photonic crystals from ZnO colloidal spheres,” *Mater. Chem. Phys.* **80**, 257–63 (2002).
- [11] M. D. Carbajal-Tinoco, G. Cruz de León, and J. L. Arauz-Lara, “Brownian motion in quasibidimensional colloidal suspensions,” *Phys. Rev. E* **56**, 6962–9 (1997).
- [12] H. Acuña Campa, M. D. Carbajal-Tinoco, J. L. Arauz-Lara, and M. Medina-Noyola, “Collective dynamics in quasibidimensional colloidal suspensions,” *Phys. Rev. Lett.* **80**, 5802–5 (1998).
- [13] R. Pesché and G. Nägele, “Stokesian dynamics study of quasi-two-dimensional suspensions confined between two parallel walls,” *Phys. Rev. E* **62**, 5432–43 (2000).
- [14] R. Pesché, M. Kollmann, and G. Nägele, “Brownian dynamics study of dynamic scaling and related freezing criteria in quasi-two-dimensional dispersions,” *J. Chem. Phys.* **114**, 8701–7 (2001).
- [15] P. Laçon, G. Batrouni, L. Lobry, and N. Ostrowsky, “Drift without flux: Brownian walker with a space-dependent diffusion coefficient,” *Europhys. Lett.* **54**, 28–34 (2001).
- [16] A. H. Marcus, J. Schofield, and S. A. Rice, “Experimental observations of non-Gaussian behavior and string-like cooperative dynamics in concentrated quasi-two-dimensional colloidal liquids,” *Phys. Rev. E* **60**, 5725–36 (1999).
- [17] J. Santana-Solano and J. L. Arauz-Lara, “Hydrodynamic interactions in quasi-two-dimensional colloidal suspensions,” *Phys. Rev. Lett.* **87**, 038302 (2001).
- [18] J. Santana-Solano and J. L. Arauz-Lara, “Short-time dynamics of colloidal particles confined between two walls,” *Phys. Rev. E* **65**, 021406–1–8 (2002).
- [19] B. Cui, H. Diamant, B. Lin, and S. A. Rice, “Anomalous hydrodynamic interaction in a quasi-two-dimensional suspension,” *Phys. Rev. Lett.* **92**, 258301–1–4 (2004).
- [20] I. Cohen, T. G. Mason, and D. A. Weitz, “Shear-induced configurations of confined colloidal suspensions,” *Phys. Rev. Lett.* **93**, 046001 (2004).
- [21] L. J. Durlofsky and J. F. Brady, “Dynamic simulation of bounded suspensions of hydrodynamically interacting

- particles,” *J. Fluid. Mech.* **200**, 39–67 (1989).
- [22] P. Nott and J. Brady, “Pressure-driven flow of suspensions—simulation and theory,” *J. Fluid Mech.* **275**, 157–199 (1994).
- [23] J. F. Morris and J. F. Brady, “Pressure-driven flow of a suspension: Buoyancy effects,” *Int. J. Multiphase Flow* **24**, 105–30 (1998).
- [24] A. Singh and P. R. Nott, “Normal stresses and microstructure in bounded sheared suspensions via Stokesian dynamics simulations,” *J. Fluid Mech.* **412**, 279–301 (2000).
- [25] J. F. Morris, “Anomalous migration in simulated oscillatory pressure-driven flow of a concentrated suspension,” *Phys. Fluids* **13**, 2457–62 (2001).
- [26] S. Bhattacharya, J. Bławdziewicz, and E. Wajnryb, “Many-particle hydrodynamic interactions in parallel-wall geometry: Cartesian-representation method,” *Physica A* **xx**, xxxx (2005).
- [27] S. Bhattacharya, J. Bławdziewicz, and E. Wajnryb, “Hydrodynamic interactions of spherical particles in suspensions confined between two planar walls,” *J. Fluid Mech.* **xxx**, xxx (2005).
- [28] R. B. Jones, “Spherical particle in Poiseuille flow between planar walls,” *J. Chem. Phys.* **121**, 483–500 (2004).
- [29] S. Bhattacharya, J. Bławdziewicz, and E. Wajnryb, “Far-field approximation for hydrodynamic interactions in parallel-wall geometry,” *J. Comput. Phys.* **xx**, xxx (2005).
- [30] M. E. Staben, A. Z. Zinchenko, and R. H. Davis, “Motion of a particle between two parallel plane walls in low-Reynolds-number Poiseuille flow,” *Phys. Fluids*. **15**, 1711–33 (2003).
- [31] S. Kim and S. J. Karrila, *Microhydrodynamics: Principles and Selected Applications* (Butterworth-Heinemann, London, 1991).
- [32] B. Cichocki, B. U. Felderhof, and R. Schmitz, “Hydrodynamic Interactions Between Two Spherical Particles,” *PhysicoChem. Hyd.* **10**, 383–403 (1988).
- [33] R. G. Cox and H. Brenner, “Effect of finite boundaries on Stokes resistance of an arbitrary particle. 3. Translation and rotation,” *J. Fluid Mech.* **28**, 391 (1967).
- [34] P. Mazur and D. Bedeaux, “A generalization of Faxén’s theorem to nonsteady motion of a sphere through an incompressible fluid in arbitrary flow,” *Physica* **76**, 235–46 (1974).
- [35] B. U. Felderhof, “Force Density Induced on a Sphere in Linear Hydrodynamics. II. Moving Sphere, Mixed Boundary Conditions,” *Physica A* **84**, 569–576 (1976).
- [36] R. B. Jones and R. Schmitz, “Mobility Matrix for Arbitrary Spherical Particles in Solution,” *Physica A* **149**, 373–394 (1988).
- [37] J. Bławdziewicz, E. Wajnryb, and M. Loewenberg, “Hydrodynamic Interactions and Collision Efficiencies of Spherical Drops Covered with an Incompressible Surfactant Film,” *J. Fluid Mech.* **395**, 29–59 (1999).
- [38] B. U. Felderhof and R. B. Jones, “Displacement theorems for spherical solutions of the linear Navier-Stokes equations,” *J. Math. Phys.* **30**, 339–42 (1989).
- [39] B. Cichocki, R. B. Jones, R. Kutteh, and E. Wajnryb, “Friction and mobility for colloidal spheres in Stokes flow near a boundary: The multipole method and applications,” *J. Chem. Phys.* **112**, 2548–61 (2000).
- [40] B. Cichocki and R. B. Jones, “Image representation of a spherical particle near a hard wall,” *Physica A* **258**, 273–302 (1998).
- [41] B. Cichocki, B. U. Felderhof, K. Hinsen, E. Wajnryb, and J. Bławdziewicz, “Friction and mobility of many spheres in Stokes flow,” *J. Chem. Phys.* **100**, 3780–3790 (1994).
- [42] L. Durlofsky, J. F. Brady, and G. Bossis, “Dynamic simulation of hydrodynamically interacting particles,” *J. Fluid Mech.* **180**, 21–49 (1987).
- [43] D. Frenkel and B. Smit, *Understanding Molecular Simulation. From Algorithms to Simulations* (Academic Press, New York, 2002).
- [44] P. Ganatos, R. Pfeffer, and S. Weinbaum, “A strong interaction theory for the creeping motion of a sphere between plane parallel boundaries. Part 2. Parallel motion,” *J. Fluid Mech.* **99**, 755–83 (1980).
- [45] S. Bhattacharya and J. Bławdziewicz, “Image system for Stokes-flow singularity between two parallel planar walls,” *J. Math. Phys.* **43**, 5720–31 (2002).
- [46] G. Ahmadi, H. F. Zhang, R. J. Han, and B. Greenspan, “Removal of particle pairs from a plane surface,” *J. Adhes.* **81**, 189–212 (2005).
- [47] Y. Han, A. Alsayed, M. Nobili, J. Zhang, T. C. Lubensky, and A. G. Yodh, “Brownian Motion of a single spheroid in water,” *xxx xxx*, xxx (xxx).
- [48] J. Bławdziewicz, V. Cristini, and M. Loewenberg, “Stokes flow in the presence of a planar interface covered with incompressible surfactant,” *Phys. Fluids* **11**, 251–258 (1999).